Comparison of Four Competing Invasion Percolation Models for Gas Flow in Porous Media

I. Banerjee[1], A. Guthke[2], C.J.C. Van De Ven[3], K.G. Mumford[4], W. Nowak[1]

[1]Institute for Modelling Hydraulic and Environmental Systems (IWS)/LS3, University of Stuttgart, Germany

[2]Stuttgart Center for Simulation Science, Cluster of Excellence EXC 2075, University of Stuttgart, Stuttgart, Germany

[3]Department of Civil and Environmental Engineering, Carleton University, Ontario, Canada

[4]Department of Civil Engineering, Queen's University, Kingston, Canada

Key Points:

- Macroscopic Invasion Percolation models may be used in transitional or continuous gas flow regimes
- Their input of randomized heterogeneous entry pressure fields plays a sensitive role
- These models are not suitable for calibrating saturation-related parameters

Corresponding author: Ishani Banerjee, `ishani.banerjee@iws.uni-stuttgart.de`

Abstract

Numerous variations of Invasion-Percolation (IP) models can simulate multiphase flow in porous media across various scales (pore-scale IP to macroscopic IP); here, we are interested in gas flow in water-saturated porous media. This flow occurs either as continuous or discontinuous flow, depending on the flow rate and the porous medium's nature. Literature suggests that IP models are well suited for the discontinuous gas flow regime; other flow regimes have not been explored. Our research compares four existing macroscopic IP models and ranks their performance in these "other" flow regimes. We test the models on a range of gas-injection in water-saturated sand experiments from transitional and continuous gas flow regimes. Using the light transmission technique, the experimental data is obtained as a time series of images in a 2-dimensional setup. To represent pore-scale heterogeneities, we ran each model version on several random realizations of the initial entry pressure field. We use a diffused version of the so-called Jaccard coefficient to rank the models against the experimental data. We average the Jaccard coefficient over all realizations per model version to evaluate each model and calibrate specific model parameters. Depending on the application domain, we observe that some macroscopic IP model versions are suitable in these previously unexplored flow regimes. Also, we identify that the initial entry pressure fields strongly affect the performance of these models. Our comparison method is not limited to gas-water systems in porous media but generalizes to any modelling situation accompanied by spatially and temporally highly resolved data.

1 Introduction

Gas flow in water-saturated porous media is a specific case of multiphase flow. The gas phase flowing through a water-saturated porous medium can be miscible or immiscible with the water phase. We explore the immiscible flow of gas in this study.

Patterns created by the immiscible flow of gas in water-saturated porous media result from an interplay between capillary forces, viscous forces, and gravitational forces (Ewing & Berkowitz, 1998; Morrow, 1979; Løvoll et al., 2005; Van De Ven & Mumford, 2019). Lenormand et al. (1988) investigated the interplay between capillary forces and viscous forces, for the immiscible flow of fluids in a porous medium, with varying viscosity ratios. They identified three immiscible flow regimes: stable displacement (when a more viscous fluid displaces a less viscous fluid), viscous fingering (when a less viscous

fluid displaces a more viscous fluid), and capillary fingering (in the absence of viscous forces). Their experiments and simulations involved multiphase flow in a horizontal setup, and the fluids used in their study did not have a considerable density contrast.

In the specific case of *gas* flow in water-saturated porous media, there is a substantial contrast in density between gas and water; thus, the influence of gravitational forces cannot be ignored. It has been observed that the interface between the fluids can be either stabilized or destabilized in the presence of gravitational forces (Glass et al., 2000; Ewing & Berkowitz, 1998; Van De Ven & Mumford, 2019; Frette et al., 1992; Glass & Yarrington, 1996; Wilkinson, 1984). For example, when a low-density fluid displaces a high-density fluid from above or when a high-density fluid displaces a low-density fluid from below in a vertical setup, buoyant forces stabilize the interface. In the other scenarios, destabilization of the interface occurs, generating fingers (*Gravity fingering*, Glass and Nicholl (1996)).

When gas is injected from below into water-saturated sand, depending on the interplay between gravitational, capillary, and viscous forces, gas-water interfaces exhibit gravity fingering combined with one or more of Lenormand et al. (1988)'s flow regimes. In the same porous medium, this combination depends primarily on gas injection rates. At low gas injection rates, the viscous effects are less relevant. Therefore, the flow is controlled by a combination of capillary forces (capillary fingering regime) and gravitational forces. Upon increasing the injection rates, the control shifts to a combination of viscous forces (viscous fingering regime) and gravitational forces. These gas flow regimes are classified as **continuous**, **transitional**, and **discontinuous**, depending on the grain size of the porous media and the rate of gas flow (Geistlinger et al., 2006). In **continuous flow** regime, the gas phase flows as a continuous phase, and in the case of **discontinuous flow** regime, gas flows as discrete gas bubbles, or clusters (Geistlinger et al., 2006; Glass et al., 2000; K. G. Mumford et al., 2009; Ben-Noah et al., 2022). The **Transitional flow** of gas has characteristics from both the continuous and discontinuous regime. As a result of the balance of forces, the gas-flow regime tends to be discontinuous at low gas-flow rates and in coarser porous media moving towards the continuous regime as the flow rate increases or for finer porous media (Geistlinger et al., 2006).

Gas flow in water-saturated porous media has been investigated using gas-injection experiments in water-saturated artificial (glass beads) as well as natural (sand) porous

media (, e.g., Ji et al., 1993; M. C. Brooks et al., 1999; Selker et al., 2006; Stöhr & Khalili, 2006; Geistlinger et al., 2006; K. G. Mumford et al., 2009, to name a few). Besides laboratory experiments, numerical models are often used for understanding multiphase flow in porous media. These models can be essential tools to encode and test hypotheses about the multiphase flow mechanisms at work and to make useful predictions for many real-world engineering applications. Both continuum and (stochastic) discrete growth models can be used. Continuum models are fully physics-based (relying on partial differential equations) with disadvantages like being slow and computationally expensive. Discrete growth models simplified abstractions of the real systems, are fast and computationally inexpensive but have comparatively stronger underlying assumptions.

Gas flow in saturated porous media is susceptible to perturbations at the pore scale. *Continuum models* require an extremely fine mesh for the numerical discretization to appropriately capture such local perturbations (Samani & Geistlinger, 2019; Oldenburg et al., 2016). This further slows down the continuum-model simulations and increases their computational cost (Glass et al., 2001; Oldenburg et al., 2016). Both laboratory experiments and numerical model formulations of a real-world system are not free from uncertainties. While laboratory experiments can have uncertainty associated with experimental control, measurements or data processing techniques, numerical models can suffer from conceptual and parameter uncertainty, affecting their prediction quality. Stochastical analysis of these real-world systems helps address these uncertainties appropriately. However, due to their computational cost and complexity, continuum models are not fit candidates for such stochastic analysis. In contrast, *discrete growth models* are ideal candidates for such analysis. Out of many discrete growth models in the multiphase literature (e.g., Diffusion limited aggregation (DLA) (Paterson, 1984; Witten & Sander, 1983), Invasion Percolation (IP) (Wilkinson & Willemsen, 1983), anti-DLA (Meakin & Deutch, 1986)), we are specifically interested IP models.

Invasion Percolation (IP) models are (stochastic) discrete growth models often used for simulating displacement of immiscible fluids through porous media in the capillary fingering regime (Lenormand et al., 1988). The term Invasion Percolation was first coined by Wilkinson and Willemsen (1983) for a pore-scale model, which incorporated phase accessibility rules to standard Percolation models of Broadbent and Hammersley (1957) to assure connectivity within a phase.

Many IP model versions with variations in the underlying rules have been developed to match the behaviour of specific fluids in specific porous media under specific conditions (, e.g., Ewing & Berkowitz, 1998, 2001; Birovljev et al., 1991; Kueper & McWhorter, 1992; Frette et al., 1992; Ioannidis et al., 1996; Glass et al., 2001; K. G. Mumford et al., 2015; Trevisan et al., 2017, to name a few). However, all of them have the following typical conceptual and numerical implementation:

1. At first, a pore network of blocks/nodes is generated with a given connectivity by assigning each pore an invasion/entry threshold selected from some distribution. This network can be 2D (2-dimensional) or 3D (3-dimensional).

2. Initially, all the blocks are occupied by the defending fluid. Then the invading fluid is injected at some point in the network. For example, in our study, *water* is the *defending* fluid, and *gas* is the *invading* fluid.

3. Pores with connection to the invaded pore are evaluated for their entry thresholds, and, based on some criterion (mostly minimum entry threshold), one of the connected blocks is then invaded.

IP models also need to incorporate buoyancy effects to simulate gas invasion in water-saturated porous media. Several studies have therefore used IP models with gravitational/buoyant force effects to model gas-water flow systems or fluid systems with significant density-difference in porous media (, e.g., Frette et al., 1992; Birovljev et al., 1991; Meakin et al., 1992; Ioannidis et al., 1996; Held & Illangasekare, 1995; Glass & Yarrington, 1996; Tsimpanogiannis & Yortsos, 2004; Cavanagh & Haszeldine, 2014; Trevisan et al., 2017, to name a few). Further, to accurately simulate gas flow from the discontinuous regime (slow gas flow rate), a rule allowing re-invasion of water into gas-filled blocks is added to the IP models (Wagner et al., 1997). This re-invasion can cause fragmentation or mobilization of the gas clusters.

The pore-scale IP models described above must be upscaled to use them for large engineering applications: like subsurface contaminant remediation, oil extraction, geologic gas storage etc.; i.e., any scale larger than the pore-scale. Studies like Kueper and McWhorter (1992); Ewing and Gupta (1993); Ioannidis et al. (1996) abstracted processes from the pore-scale IP model to then use them at the larger scales of their problems. The Near-Pore Macro-Modified Invasion Percolation (NP-MMIP) model of Glass et al. (2001) is one such macroscopic IP model used to simulate carbon dioxide injection in a water-

saturated macro-heterogeneous porous media. In the work of Glass and Yarrington (2003), an upscaled rule for pore-scale re-invasion of water was added to NP-MMIP to simulate gas flow in the discontinuous regime. In these macroscopic IP models, the model blocks represent a network of pores instead of single pores.

Traditional IP models, at any scale, do not incorporate viscous effects and have not been tested before in gas flow regimes other than discontinuous flow (slow-injection of gas): the transitional and continuous gas flow regimes. Experimental data from gas injection in homogeneous water-saturated sand shows that, with increasing gas injection rate, viscous forces dominate the injection zone, making the gas flow radial around the injection point (Selker et al., 2006; Van De Ven & Mumford, 2019). However, once the gas propagates further away from the injection point, gravitational effects overcome the viscous effects (Van De Ven et al., 2020). Hence, the upward movement of gas is observed as multiple fingers (referred to as gravity fingering in Glass and Nicholl (1996)). Thus, at higher gas injection rates, ignoring viscous effects near the gas injection point as in traditional IP models is not a valid assumption.

The addition of several rules to IP models makes them potential candidates for transitional or continuous flow regimes. For example, Glass et al. (2001) used an invasion of more than one block per step for their NP-MMIP model, adding more gas volume per invasion step. This rule is supported by evidence from their gas-injection experiments (Glass et al., 2000) that more gas is pushed into the system for a higher injection rate, and more than one finger is produced. Further, Ewing and Berkowitz (1998) developed a generalized growth model for dense non-aqueous phase liquid (DNAPL) migration at the macroscopic scale by including invasion rules to capture viscous effects. The rule for stochastic selection in the Stochastic Selection and Invasion (SSI) model of Ewing and Berkowitz (1998) was adapted to use in simulating gas migration in water-saturated homogeneous sand (K. G. Mumford et al., 2015).

In general, numerical models must be compared to experimental data sets to test, calibrate and validate their underlying hypotheses, leading to their refined formulations. Although traditional macroscopic IP models are designed for use in regimes of low gas flow rate, our goal is to test their performance in the transitional and continuous flow regimes, from which direction for further model refinement can be derived. Thus, we use four models in this study:

1. NP-MMIP model of Glass et al. (2001) without viscous modifications.

2. Macro-IP model involving the rule for re-invasion of water (Glass & Yarrington, 2003; K. G. Mumford et al., 2015).

3. A combination of Macro-IP model with the rule of more than one invasion block per step (including the original viscous modification as in Glass et al. (2001)).

4. A combination of Macro-IP model and modified stochastic selection rule of SSI model of Ewing and Berkowitz (1998) adapted from K. G. Mumford et al. (2015).

These IP models at a macroscopic scale have been compared to experiments individually and each at a certain flow regime, but no study has performed an inter-comparison of these model hypotheses using experimental data (across all three regimes of gas flow: continuous, transitional and discontinuous).

Thus, in this work, we test four different macroscopic IP model versions with data from nine gas-injection experiments in homogeneous water-saturated sand. These experiments belong to the transitional and continuous gas flow regimes (Van De Ven & Mumford, 2019), controlled by varying the injection rate. Thus, we assess the model performance under gas-flow conditions other than the discontinuous or slow-gas flow regime. In our previous work (Banerjee et al., 2021), we developed and tested a quantitative method of comparison between IP-type models and laboratory gas-injection data from the discontinuous flow regime. In Banerjee et al. (2021), we demonstrated our method using a single macroscopic IP model based on K. G. Mumford et al. (2015). Now, we use this method to test and rank the four macroscopic IP model versions for gas flow from continuous and transitional regimes. Our key research questions are:

1. Can any of these models be used for simulating gas flow in the continuous or transitional flow regimes?

2. If yes, which ones are more suitable?

3. What can we learn from the comparison of more or less successful model strategies and their remaining weaknesses to derive recommendations for future modelling efforts?

We organize our model comparison study as follows. At first, we introduce the experiments and describe the formulation of the four macroscopic IP model versions used in this study in Section 2. Then, in Section 3, we detail the method or tool of compar-

ison we use for evaluating and ranking the models against the experimental data. Also,

we discuss the overall implementation of the method for the inter-comparison of models in Section 3. We report the results from this implementation and provide insights about the model performance and its parameters in Section 4. Finally, we summarize our conclusions and recommendations for future work in Section 5.

2 Experiments and Models

In this section, we describe the experimental data sets (Section 2.1) and the four macroscopic IP model versions (Sections 2.2-2.3) used for our model comparison study. All four model versions are at the same scale and share some similarities. Fig. 1 shows the conceptual building of the 4 model versions used in this study. To facilitate the understanding of the models, first, we describe the model version (we call it **Model 1**) based on the NP-MMIP of Glass et al. (2001) (Section 2.2). Model 1 does not include the modifications for viscous effects from the NP-MMIP model of Glass et al. (2001). Then, in Section 2.3, we introduce **Model 2**, which has additional rules of re-invasion of water at the macroscopic scale, same as in Glass and Yarrington (2003); K. G. Mumford et al. (2015) (see Fig. 1). **Model 3** (Section 2.4) is a combination of Model 2 and a rule for producing thicker fingers from the viscous modification of NP-MMIP model of Glass et al. (2001) (see Fig. 1). Finally, **Model 4** in Section 2.5, which is built by combining Model 2 and a modified rule for stochastic invasion from Ewing and Berkowitz (1998) (see Fig. 1). Model 4 is based on K. G. Mumford et al. (2015). All the model versions used here generate binary images (gas-presence/gas-absence) as output.

2.1 Experiments

For this study, we use nine gas-injection experiments from Van De Ven and Mumford (2019), which were conducted in triplicate at 10ml/min (10-A, 10-B, 10-C), 100ml/min (100-A, 100-B, 100-C) and 250ml/min (250-A, 250-B, 250-C). The gas flow patterns of the different regimes are distinguished using the ratio of Bond number, Bo (ratio of gravitational force to capillary force) to Capillary number, Ca (ratio of viscous force to capillary force) (Van De Ven & Mumford, 2019). The triplicate experiments at 10ml/min (10-A, 10-B, 10-C) belong to the transitional flow regime, with $Bo/Ca = -1.61 \times 10^2$ (Van De Ven & Mumford, 2019). The triplicate at 100ml/min (100-A, 100-B, 100-C) with $Bo/Ca = -1.61 \times 10^1$ and at 250ml/min (250-A, 250-B, 250-C) with $Bo/Ca = -6.45 \times$
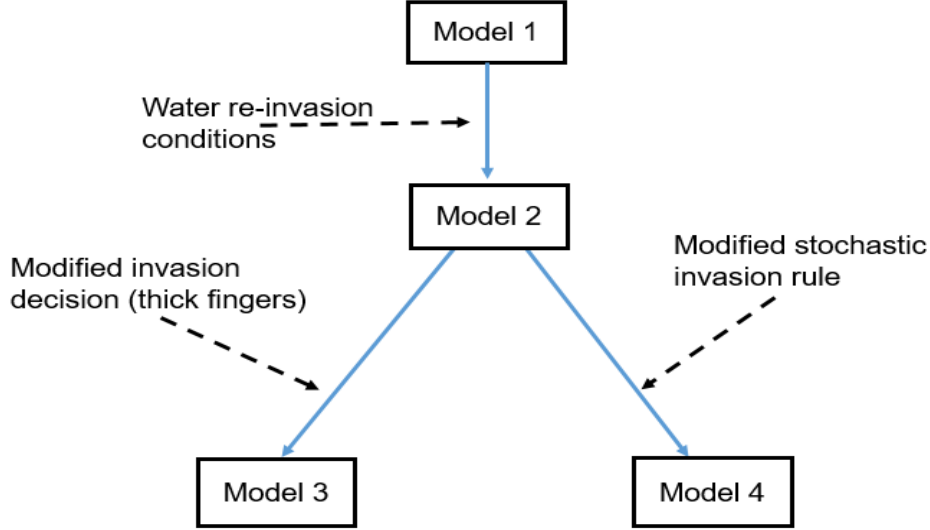
Figure 1. Flowchart illustrating the building process of the competing model versions of this study.

10^0 belong to the continuous flow regime, with increasing influence of viscous forces (Van De Ven & Mumford, 2019). The experimental setup and data processing details are found in Van De Ven and Mumford (2019). We present a summary of the data relevant to understanding our study.

Gas (air) is injected in water-saturated homogeneous sand (grain size 0.713±0.023 mm), filled into a quasi-2D acrylic cell of dimensions 250mm ×250mm ×10 mm. A continuous wet-packing procedure was used to ensure that the resulting sand distribution was homogeneous and free of trapped gas. Air was then injected into the saturated sand packs at the defined rates of 10, 100 and 250 ml/min using a syringe pump. To ensure that no grain rearrangement occurred during injection, a confining lid was placed at the top of the system. The gas movement and resulting gas presence within the sand pack were measured using the light transmission method (Niemet & Selker, 2001; Tidwell & Glass, 1994). In this method, the back of the cell is lit, and intensity images are collected at a specific frame rate for the total duration of the experiment. Individual pixel intensity values of these raw images are averaged over a block size of 1×1 mm, and the intensity values of the block are used to calculate the optical density (OD) (Kechavarzi et

al., 2000) values. For any block, OD > 0.02 is considered as the presence of gas. We thus obtain a time series of binary (gas/no gas) images.

Please note that, for the experimental replicates at a particular injection rate, the sand is washed and repacked with the same procedure to obtain a homogeneous packing after each experiment. Nevertheless, with a new arrangement of all grains, each experimental outcome is unique. The final time images for the nine experiments used in this study are shown in Fig. 2. Note, for experimental triplicate at an injection rate of 10ml/min (first row of Fig. 2), the gas finger of 10-B moves towards the side of the domain, instead of being centrally aligned like in 10-A and 10-C. Also, for experiment 100-A (second row of Fig. 2), the multiple gas fingers are quite spread out, but those in 100-C merge to produce thicker fingers along the way (second row of Fig. 2). These differences in the images support the uniqueness of each experimental outcome owing to the re-packing of the sand.

2.2 Model 1

Our Model 1 is based on the NP-MMIP model of Glass et al. (2001), briefly introduced in Section 1. We adopt a 2D grid description of the porous medium in accordance with the experimental data. In this model, the gas is placed at the injection block (position of the gas injection needle in the experiment), and the invasion thresholds (T_e) [cm of H_2O] of the neighbouring blocks are calculated:

$$T_e = P_e + P_w, \tag{1}$$

where P_e is the local entry pressure of the block [cm of H_2O], and P_w is the pressure of the water phase [cm of H_2O]. P_e is the specific value of capillary pressure (P_c) required by gas to percolate a water-occupied block. P_w incorporates the buoyant effects and is calculated assuming hydrostatic conditions:

$$P_w = \rho_w g z. \tag{2}$$

Here, ρ_w is the density of water [kg/m^3], g is the acceleration due to gravity [m/s^2], and z is the height [m] from the top of the acrylic glass cell. At each model step, the neighbouring block with the minimum invasion threshold (T_e) is invaded by gas.
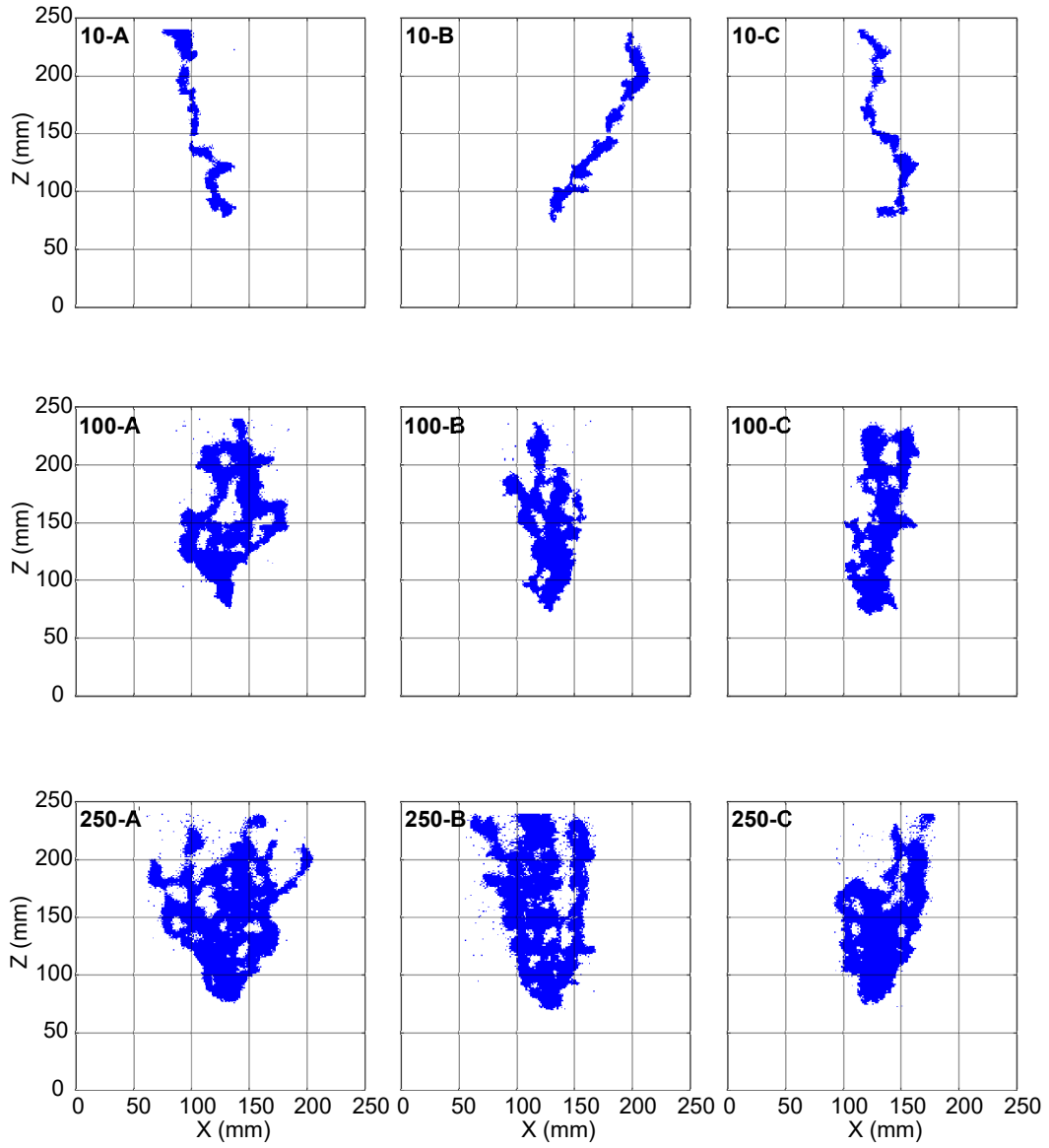
Figure 2. Final time binary experimental images for experiments 10-A, 10-B, 10-C, 100-A, 100-B, 100-C, 250-A, 250-B, 250-C. These gas presence/absence images are not free from pixel noise. Zones of the images where too many noisy pixels aggregate have been cleaned prior to use in this study.

281 The P_e field of a porous medium depends on the pore-scale arrangement of the solid

282 and its interaction with the fluids. A precise measurement of the P_e field at the scale of

283 our experiments (block size of 1mm x 1mm) is practically impossible. Therefore, it is

284 typical to use random P_e fields, i.e. a randomly generated value per block. Since P_e is

285 a point on the capillary pressure (P_c)–saturation (S) curve, we randomly sample the P_e

286 values that we assign individually to all model blocks, using the Brooks-Corey $P_c - S$

287 relationship (R. Brooks & Corey, 1964) for our material of interest (homogeneous sand

288 of 0.7mm average grain size):

$$S_e = \left(\frac{P_c}{P_d} \right)^{-\lambda}. \tag{3}$$

290 Here, S_e is the effective wetting phase saturation (R. Brooks & Corey, 1964), P_c

291 is capillary pressure [cm of H_2O], P_d is the macroscopic displacement pressure [cm of

292 H_2O], and λ is the pore-size distribution index. The value of λ varies typically between

293 1-4 and can be up to 7 for very uniform sands. We sample the P_e values from the inverse

294 of the cumulative distribution function of P_c (using Equation 3):

$$P_e = P_d \mathcal{U}^{-\frac{1}{\lambda}}. \tag{4}$$

296 Here, $\mathcal{U}$ is a random number from the standard uniform distribution on the inter-

297 val $[0, 1]$. This sampling method is called the Inverse Transform sampling method, which

298 has been used in the works of Glass et al. (2001); K. G. Mumford et al. (2015); Baner-

299 jee et al. (2021). The P_e values thus assigned to the blocks are not spatially correlated,

300 but this extension could easily be achieved via geostatistical simulation.

301 ### 2.3 Model 2

302 Our Model 2 has the same setup and follows the same rules for invasion of gas as

303 specified for Model 1 (Section 2.2). This means it follows Equations 1 — 4 and also obeys

304 the rule of invading the neighbouring block with the minimum T_e. Furthermore, it has

305 a rule for re-invasion of water into gas-occupied blocks to simulate the fragmentation and

306 mobilization events observed for discontinuous gas flow (Glass & Yarrington, 2003; K. G. Mum-

307 ford et al., 2015; Banerjee et al., 2021). This rule is an upscaled version of the re-invasion

308 rule of the pore-scale model of Wagner et al. (1997).

In Wagner et al. (1997), the re-invasion of water into the gas-filled pores is realized by a withdrawal pressure threshold. At the scale of our model, the threshold for re-invasion, also known as the terminal threshold (T_t) [cm of H_2O], is calculated as the summation of the terminal pressure (P_t) [cm of H_2O] and the hydrostatic pressure (P_w).

$$T_t = P_t + P_w. \tag{5}$$

P_t is calculated using the P_e- to $-P_t$ ratio (α) obtained from the characteristic drainage and imbibition curves for the porous medium of interest, which takes capillary-pressure hysteresis into account (Gerhard & Kueper, 2003; K. G. Mumford et al., 2009).

$$P_t = \alpha P_e \tag{6}$$

Water re-invades a gas-occupied block if:

$$T_{t,g} > T_{e,w}, \tag{7}$$

where g and w stand for gas- and water-occupied blocks, respectively (K. G. Mumford et al., 2015). In the model, this rule is implemented by comparing the maximum of the $T_{t,g}$ values of the gas cluster with the invasion threshold value of the most gas invasion favourable neighbouring water-occupied grid block (minimum T_e value). When water re-invades a gas-occupied block, the model assumes that it completely expels gas from that block. If the re-invasion of water occurs in blocks on the periphery of the gas cluster, mobilization occurs. If the re-invasion causes a disconnection in the gas cluster, fragmentation occurs. A gas cluster is allowed to grow (based on the rules of Model 1) only when connected to the gas cluster containing the injection point. Thus, only re-arrangement of blocks is possible for gas clusters disconnected from the injection point.

2.4 Model 3

Our Model 3 includes an invasion rule of Glass et al. (2001) into our Model 2 implementation. In this regard, our model formulation follows the rules specified by the Equations $1 - 7$. The difference is that multiple neighbouring blocks (nb) are invaded instead of one block per step. This means that not only the easiest-to-invade block is in-

335 vaded, but the nb easiest ones among all candidate blocks. This weakens the influence

336 of T_e and hence resembles a reduced dominance of capillary effects in favour of viscos-

337 ity effects. The number of blocks to invade is chosen by observing the gas fingers from

338 the experimental data.

339   Please note that, in our implementation, the number of blocks invaded is chosen

340 dynamically until the number of blocks specified at the beginning of the simulation is

341 available for invasion. For example, in a model run specified to invade $nb = 10$ blocks

342 per step, initially, when the number of available neighbours is < 10, all the available ones

343 are invaded. Ten neighbouring blocks are invaded only when the gas cluster around the

344 injection point is big enough to have ≥ 10 neighbouring blocks. After the invasion of

345 multiple blocks, fragmentation and mobilization is carried out in a similar manner as de-

346 scribed in Model 2. This means that the simulation of the fragmentation and mobiliza-

347 tion event in Model 3 does not involve gas invasion of multiple water-occupied neighbour-

348 ing blocks.

2.5 Model 4

350   Model 4 is implemented following the formulations specified by Equations $1 - 7$.

351 Model 2 selects the neighbouring block with a minimum invasion threshold (T_e) for in-

352 vasion. In contrast, in Model 4, the neighbouring block is chosen using a modified rule

353 for stochastic selection from the Stochastic Selection and Invasion (SSI) model of Ewing

354 and Berkowitz (1998). This rule allows gas to invade not strictly only the block with the

355 minimum invasion threshold (T_e) but also less easy-to-invade blocks based on a partially

356 randomized choice. The difference between Model 3 and Model 4 is that Model 3 dimin-

357 ishes the influence of T_e deterministically for many blocks per step, while Model 4 achieves

358 the same stochastically for a single block per step.

359 In the modified rule for stochastic selection:

360   1. The list of T_e values of the neighbouring blocks (n) of the gas cluster are arranged

361   in an ascending order $T_{e,asc}$ and the cumulative sum $T_{e,cum}$ is evaluated:

$$T_{e,cum}[i] = \sum_{j=1}^{j=i} T_{e,asc}[j]; i = 1, 2, 3, \ldots, n. \tag{8}$$

362   2. Then the first block (value of i) where the rule specified by Equation 9 is found

363   true is invaded by the gas:

$$T_{e,cum}[i] > \mathcal{R}^c \sum_{j=1}^{j=n} T_e[j]. \tag{9}$$

364   Here, $\mathcal{R}$ is a uniformly distributed random number between $[0,1]$ and c is the cell

365   selection weighting factor (Ewing & Berkowitz, 1998). Please note that although

366        $\mathcal{R}$ and $\mathcal{U}$ from Equation 4 are from the same distribution, their seed numbers and

367   generator types are different. Hence we use different symbols here.

368   In the stochastic selection rule, c controls the strength of randomness, and its value

369   lies in the range of $(0, \infty)$. When $c \to \infty$, the value of $\mathcal{R}^c \to 0$ for almost all values

370   of $\mathcal{R}$. In this case, the first block on the list of $T_{e,asc}$ (block with the lowest T_e value)

371   will be invaded deterministically by gas. The resulting lightning-bolt-like gas finger is

372   the same as the gas finger generated by Model 2. In fact, for $c \to \infty$, Model 4 becomes

373   identical to Model 2. However, the lower the c value, the higher the RHS of Equation

374   9, which ensures that the higher $T_e[j]$ are picked more often; this generates gas fingers

375   that are not moving strictly upward, but have a wider spatial distribution. Please note

376   that the re-invasion of water events that result in fragmentation or mobilization of gas

377   clusters are carried out exactly as in Model 2, i.e. without any stochastic modification.

378   Table 1 shows the model parameter values used in this study.

379   The conceptual difference in the model versions is illustrated using a schematic in

380   Fig. 3. Fig. **3b** displays a gas invasion event in Model 1, which gives rise to a lightning-

381   bolt-like gas finger. The fragmentation of the gas cluster owing to water re-invasion, as

382   per Model 2, is shown in Fig. **3c**. Fig. **3d** shows the gas invasion of three blocks (three

383   most favoured blocks according to T_e values) in the injection cluster following a fragmen-

384   tation event, according to Model 3. Fig. **3e** displays the invasion of a randomly chosen

385   neighbouring block (not the most favourable block according to the T_e values) follow-

386   ing a fragmentation event according to Model 4.

387   We will show outputs generated by the Models $1-4$ with best fit to experimental im-

388   ages from 10-A, 100-A and 250-A in Section 4.

Table 1.   Model parameters used in this study.

Parameters [Units]	Symbols	Values
Common for models 1-4		
Density of water [kg/m^3]	ρ_w	1000
Acceleration due to gravity [m/s^2]	g	9.82
Average $P_t - P_e$ ratio [-]	α	0.6 (K. G. Mumford et al., 2009)
Displacement pressure [cm of H_2O]	P_d	8.66 (Schroth et al., 1996)
Pore-Size distribution index [-]	λ	5.57 (Schroth et al., 1996)
Model domain size [mm^2]	$X - Z$	250×250
Block discretization [mm^2]	$x - z$	1×1
Model 3 specific		
Number of blocks to invade	nb	$\{1, 2, ...10, 15, 20\}$ for experiments at 10ml/min
		$\{1, 2, ...20, 25, 30, 35, 40, 50\}$ for experiments at 100ml/min and 250ml/min
Model 4 specific		
Cell selection weighting factor	c	$\{5, 10, 15, 200, 500\}$

3 Method of Comparison

We begin with a summarized description of our comparison method (Section 3.1), the details of which are in Banerjee et al. (2021). Then, we list the blur-radii chosen for the Diffused Jaccard coefficient in this study in Section 3.2. After that, we enumerate the steps of our model comparison study using the (Diffused) Jaccard Coefficient in Section 3.3.
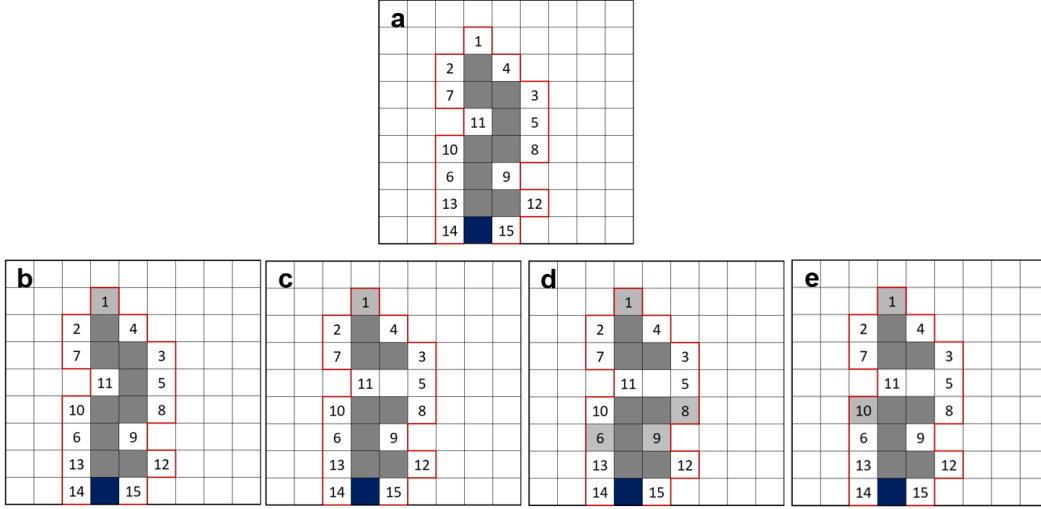
Figure 3. Illustration of the conceptual difference between the four model versions: **a** is an initial state of gas occupation in the domain, and the numbers denote the increasing order of preference of gas invasion for the neighbouring blocks in the next step based only on T_e values; **b** displays gas filling in the next step according to Model 1; **c** displays fragmentation of gas cluster in the next step according to Model 2; **d** displays a fragmentation event followed by an invasion event involving three invasion blocks ($nb = 3$) according to Model 3; **e** displays a fragmentation event followed by an invasion event according to Model 4. Light grey cells are the blocks chosen by the respective model version, and the blue block is the injection site.

3.1 Experiment-Model Comparison by (Diffused) Jaccard Coefficient

In Banerjee et al. (2021), we developed a method to compare IP-type models to image-based data. We used the method to compare a macroscopic IP model (Model 2 of this study) with a gas-injection experimental data set from the discontinuous regime.

Comparing IP-type models to laboratory or field data is challenging because they do not involve a time description. We overcome this challenge by implementing a volume-based time matching, where the volume of gas at each time step of the experiment (V_{exp}) is evaluated:

$$V_{exp}(t) = \sum_{t=t_{exp}}^{t=t_{end}} Q_{exp} \times t; t = t_{exp}, 2 \cdot t_{exp}, 3 \cdot t_{exp}, ...t_{end}, \tag{10}$$

and volume of gas per model loop counter (V_{model}) is evaluated as:

$$V_{model}(n_c) = \sum_{n_c=1}^{n_c=n_{top}} n_{blocks} \times \phi \times S_g \times V_{block}; n_c = 1, 2, 3, ... n_{top}. \qquad (11)$$

Here, Q_{exp} is the gas-injection rate of the experiment [volume/time], t_{exp} is the time step in between the capture of two successive images in the experiment, t_{end} is the time when the experiment ends, n_{blocks} is the number of blocks invaded per loop counter n_c of the model, n_{top} is the model loop counter when the gas reaches the top of the domain, V_{block} is the volume of each discretized block of the model, ϕ is the porosity, and S_g is the gas saturation value assigned to the entire gas cluster based on the values observed in the experiments (Banerjee et al., 2021). We search the nearest neighbour in the V_{exp} vector for all the time-wise elements in the V_{model} vector. Then, we assign the experimental time to the corresponding nearest-neighbour model loop counter.

After the volume-based time matching of the model output and the experimental data, we use the (Diffused) Jaccard coefficient to assess the fit quality between the model and the experimental data (images). As per the set theory, for two sets A and B, the Jaccard coefficient (J) is defined as:

$$J(A, B) = \frac{|A \cap B|}{|A \cup B|}. \qquad (12)$$

The Jaccard coefficient ranges between zero (implies: no similarity) and one (implies: complete similarity). For binary images (pixel values of gas present $= 1$ and gas absent $= 0$), it is calculated by counting the number of overlapping pixels (value 1) between two images and dividing it by the combined total number of gas presence (value 1) pixels in both the images, without double counting the already overlapped pixels (see Banerjee et al. (2021) for details).

A pixel-by-pixel comparison as in Equation 12 could reject a perfect model due to minor offsets between experiment and model, which might be within the tolerance of some real-world applications (Banerjee et al., 2021). To avoid a strict pixel-by-pixel comparison of the images, we use a Diffused Jaccard coefficient (J_d) instead of the Jaccard coefficient. To compute the Diffused Jaccard coefficient, we blur the time-matched images from the experiment and the model using Gaussian blurring by convoluting the images with a Gaussian kernel of specified width (standard deviation σ):

$$G(x, z) = \frac{1}{2\pi\sigma^2} e^{-\frac{x^2+z^2}{2\sigma^2}}, \tag{13}$$

The σ value in Equation 13 is altered to increase or decrease the blurring radius. We specify the unit of blur-radius as the kernel size relative to the original domain size of the image. The blurring leads to non-binary pixel values in the images. Therefore, we evaluate the Diffused Jaccard coefficient (J_d) for the sets $A = \{a_k : a \in R, k = 1, 2, ...n_p\}$ and $B = \{b_k : b \in R, k = 1, 2, ...n_p\}$ using the non-binary formulation of the Jaccard coefficient (also referred to as Ruzicka similarity coefficient (Deza & Deza, 2016)):

$$J_d(A, B) = \frac{\sum_k^{n_p} \min(a_k, b_k)}{\sum_k^{n_p}, \max(a_k, b_k)} \tag{14}$$

where a_k and b_k are the grey-scale values of the originally black-white (binary) images from experiments and models. For simplicity, we restrict our analysis to the final (last in time) experimental images and the corresponding model images.

3.2 Blur-radii for Diffused Jaccard Coefficient

Further, we choose three different blur-radii for the Diffused Jaccard coefficient as a performance metric for ranking the models in this study.

1. **Low blur:** We choose this blur-radius such that images from the experiments (see, Fig. 2) lose the sharpness of the pixels but do not lose their identity, i.e. the different blurred experimental-images look different. This corresponds to any application where we forgive errors in individual pixel values but insist on a close match in shape (Low blur row of images in Fig. 4). The chosen value of σ for this blurring is 1.2% of the domain size, i.e. image width. The Diffused Jaccard coefficient calculated using this blur radius is denoted as *Diffused Jaccard coefficient (low)* (J_d^{low}) in this study.

2. **Medium blur:** We choose this blur-radius such that images from the experimental triplicate at any injection rate (each row of Fig. 2) look similar, but that the images across different injection rates look different. This corresponds to applications where it is sufficient to identify diversion by flow-inhibiting structures and the overall direction of the growing finger (Medium blur row of images in Fig. 4). The chosen value of σ for this blurring is 4% of the domain size. Please note that

it is not entirely attainable, e.g., when a finger, like in experiment 10-B, favours a particular direction of flow, no amount of blurring can make it look like fingers from 10-A or 10-C where the flow is clearly in the centre of the cell. The Diffused Jaccard coefficient calculated using this blur radius is denoted as *Diffused Jaccard coefficient (med)* (J_d^{med}) in this study.

3. **High blur:** We choose this blur-radius such that images from all the experiments (Fig. 2) lose the individual details in finger structure and start looking similar. This corresponds to any application where one is interested only in the macroscopic direction of the gas finger and in no further details (High blur row of images in Fig. 4). The chosen value of σ for this blurring is 8% of the domain size. Please note again that the images from all experiments cannot look the same with any meaningful blur radius. The higher flow rates have multiple fingers and more gas in the system and can thus handle more blurring than the lower injection rate experiments that generate a single finger. The Diffused Jaccard coefficient calculated using this blur radius is denoted as *Diffused Jaccard coefficient (high)* (J_d^{high}) in this study.

In Fig. 4, we show the resulting images of the experiments 10-A, 100-A, and 250-A, with and without the blurring.

3.3 Steps of Model Comparison Study

We present an overview of the model-comparison setup in Fig. 5.

We have four competing model versions as described in Sections 2.2-2.5. In step ②, we run the models over several (500) invasion threshold (T_e) realizations for all model versions (including the sub-versions discussed below) to appropriately account for the uncertainty involved with the entry threshold (T_e) fields.

Prior to this, step ① requires some parameter specifications. We run Model 3 (Section 2.4) for varying numbers of blocks to invade (nb) at each step, creating many sub-versions of this model to test the best-fitting value. At injection rates of 100ml/min and 250ml/min, we expect a higher number of blocks to perform well because there is a high volume of gas injected into the system. We set the range of nb by visual inspection. For the experiments at injection rate of 10ml/min, nb takes the values $\{2, 3, 4, ...10, 15, 20\}$. We assign values of $\{2, 3, 4, ...20, 25, 30, 35, 40, 50\}$ to nb for the experiments at injection
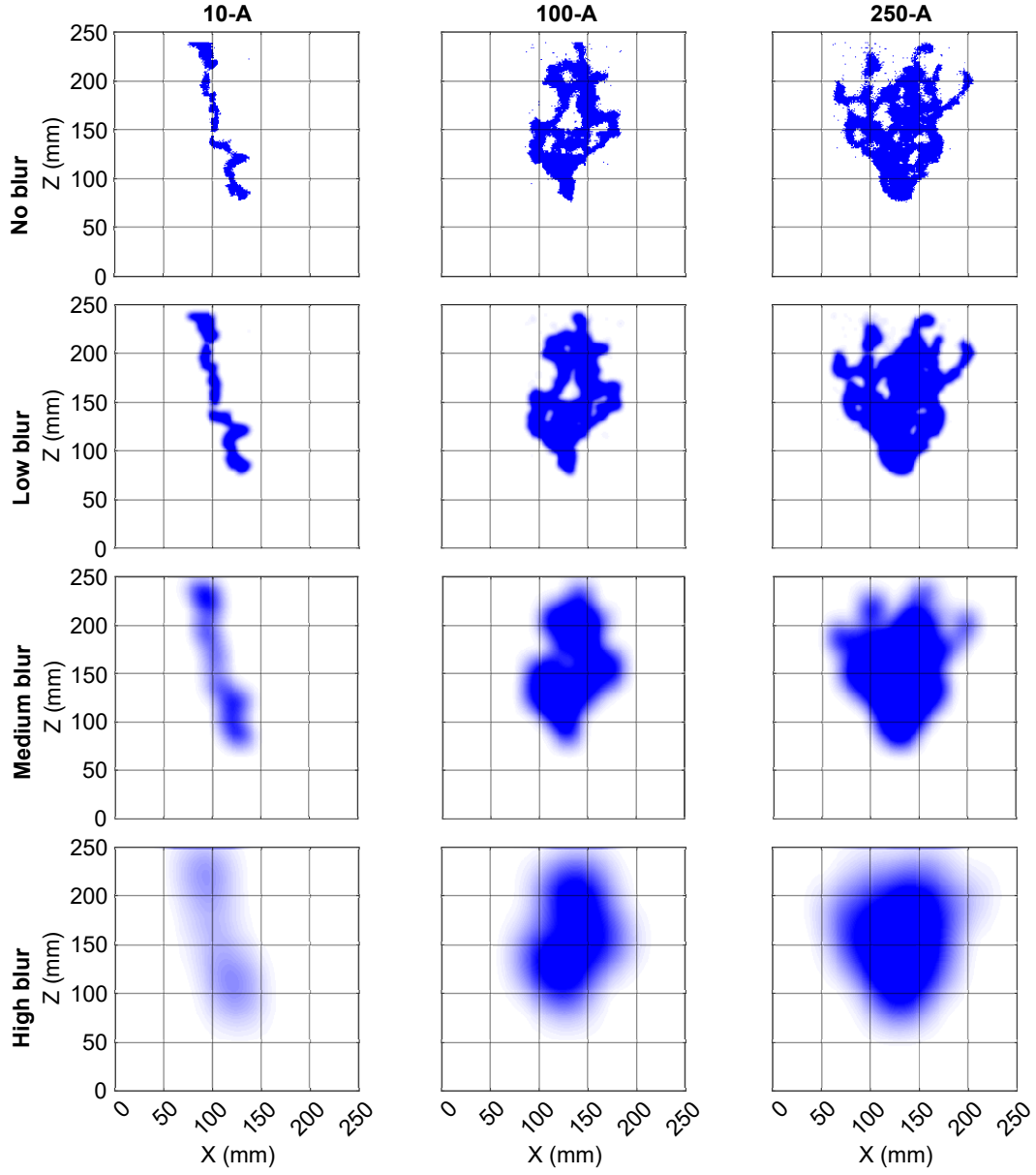
Figure 4. Final experimental image for experiments 10-A, 100-A and 250-A. Row 2-4 contains the blurred version of the images of Row 1 for the three different blur-radii.
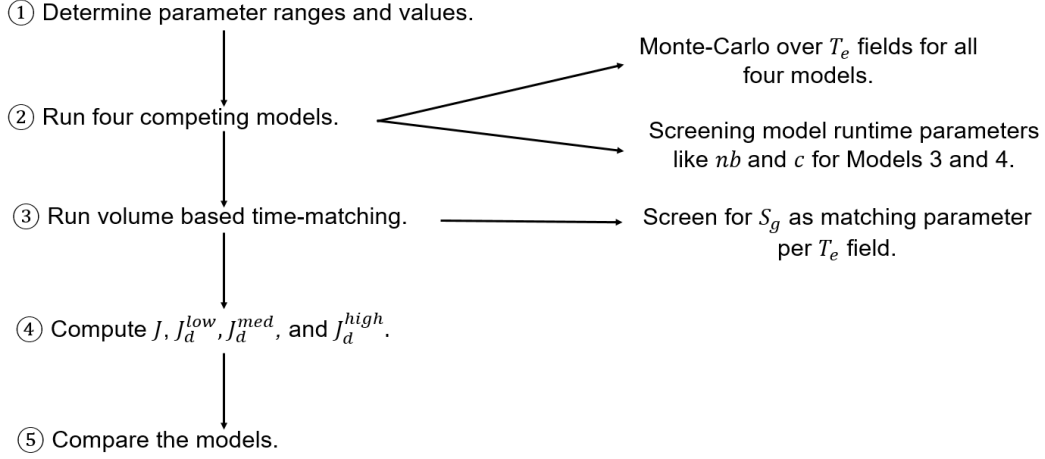
Figure 5. Flow chart listing the steps of the model-comparison setup.

rates of 100ml/min and 250ml/min. Please note that larger nb values (> 50 blocks per step) would lead to inflated circular shapes instead of multiple gas fingers, and hence $nb = 50$ was set as the upper limit.

Further, we run Model 4 (Section 2.5) for some representative c values: $\{5, 10, 15, 200, 500\}$ creating five sub-versions of this model to test the best-fitting value. We suppose that, while the transitional flow regime (10ml/min) would prefer higher c values (200 or 500), the continuous flow regime (100ml/min and 250ml/min) would prefer low c values, because low c values allow the gas to spread more laterally instead of strictly moving upwards. Please also note here that we ran the simulations for $c < 5$ values as well. But this did not lead to systematic improvements or more insightful results, so we excluded them from further analysis due to their very long runtime. Further, this study does not aim to formally optimize the c value for specific model variants with an extensive search over the feasible parameter space.

In step ③, we run the time matching procedure for all the model versions and sub-versions mentioned above. Additionally, to calibrate gas saturation values assigned per block of the model domain within the time matching, we conduct the time-matching by varying the S_g values in Equation 11 in the range of $0.02-0.44$ (in accordance with experimentally observed gas saturation values of Van De Ven et al. (2020)). In step ④, we compute the J, J_d^{low}, J_d^{med}, and J_d^{high} values to assess the quality of fit between the experimental images and the corresponding time matched model images. Per T_e field re-

alization, we want the model to choose its most suitable saturation value based on the maximum metric value. Also, these metrics are used for comparing the performance of the competing model versions.

4 Results and Discussion

We assess the performance of all four models (Section 2.2 - 2.5) and comment on their ranking (Section 4.1) for the different experiments (from Section 2.1) using the Jaccard coefficient and Diffused Jaccard coefficients enumerated in Section 3.2. In our discussion, we use the term "metric" to address the Jaccard coefficient and the three levels of Diffused Jaccard coefficient (low, med, high) altogether. We further support our deductions from the metric-based ranking by visual evidence in Section 4.2. In Section 4.3, we discuss the importance of the random entry threshold fields as model input. Also, we discuss the results from calibration of the gas-saturation parameter in the models in Section 4.4. Finally, we summarize our findings from this model selection study in Section 4.5

4.1 Overall Ranking of Models

We begin the discussion by commenting on the overall ranking of the competing models based on the maximum metric value out of the 500 Te field runs. The table specified by Fig. 6 shows that for all metric values and across most experiments, Model 1 and Model 2 rank poorly compared to Model 3 and Model 4. This is entirely expected for the experiments of the continuous flow domain (with injection rates 100 ml/min and 250 ml/min) because Model 1 and Model 2 do not include rules incorporating the gas-fingering behaviour (viscous effects, multiple fingers etc.) at these injection rates.

In the transitional flow domain (10 ml/min experiments), gas flow behaviour already shows characteristics of the continuous flow regime (Van De Ven & Mumford, 2019), where capillary forces do not entirely dominate over the viscous forces (Section 1). Recall from Sections 2.2 and 2.3 that Models 1 and 2 do not account for viscous effects and are completely formulated to be operated in the slow gas flow regime (discontinuous flow). Therefore, we note that the contrast in performance between Models (1,2) and (3,4) is higher for higher injection-rate experiments (the difference in metric values is higher for 100ml/min and 250ml/min in the table specified by Fig. 6). On that account, for the

Injection rate	10 ml/min				100ml/min				250ml/min				
Models	1	2	3	4	1	2	3	4	1	2	3	4	
A	0.207	0.187	0.297	0.225	0.110	0.106	0.446	0.381	0.083	0.080	0.439	0.422	Jaccard coefficient
B	0.135	0.129	0.168	0.178	0.142	0.137	0.494	0.392	0.090	0.086	0.535	0.408	
C	0.141	0.138	0.185	0.161	0.144	0.137	0.486	0.366	0.107	0.103	0.417	0.423	
A	0.338	0.325	0.473	0.372	0.133	0.130	0.541	0.453	0.096	0.092	0.521	0.496	Diffused Jaccard coefficient (low)
B	0.234	0.227	0.308	0.278	0.201	0.191	0.612	0.488	0.109	0.098	0.644	0.491	
C	0.265	0.260	0.320	0.271	0.173	0.169	0.620	0.474	0.134	0.130	0.490	0.491	
A	0.493	0.474	0.713	0.628	0.164	0.154	0.670	0.604	0.112	0.104	0.605	0.605	Diffused Jaccard coefficient (med)
B	0.384	0.364	0.490	0.471	0.238	0.218	0.747	0.615	0.122	0.110	0.758	0.623	
C	0.463	0.449	0.539	0.478	0.203	0.188	0.784	0.578	0.148	0.142	0.572	0.610	
A	0.527	0.501	0.821	0.700	0.175	0.158	0.758	0.753	0.120	0.107	0.674	0.700	Diffused Jaccard coefficient (high)
B	0.458	0.422	0.639	0.617	0.244	0.218	0.827	0.715	0.122	0.110	0.842	0.705	
C	0.584	0.551	0.725	0.709	0.216	0.194	0.873	0.663	0.152	0.145	0.652	0.633	

(Left vertical label: Triplicate Experiments. Right color bar: better / worse)
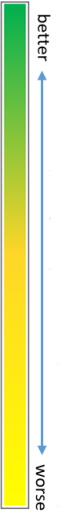
Figure 6. Table containing the maximum metric value for each model version out of the 500 Te field runs and for the best gas-saturation (S_g) value (see Section 4.4). For Model 3 and Model 4, the metric corresponds to the respective best parameter value (see Table 2).

entire transitional and continuous flow regime, we do not recommend the use of Model 1 and Model 2. Overall, in our study, Model 3 emerges as the best-performing model for most experiments and metrics, always (and often closely) followed by Model 4.

The blurring of the images does not change the overall ranking of the models across all investigated scales of interest. The difference in the model outputs occurs (e.g. finger width, finger direction etc.) even on larger scales. We discuss the effect of blurring further when we discuss the models' relative performance across all 500 T_e field realizations (see Section 4.1.2).

4.1.1 What about the Parameter Values of Models 3 and 4?

Models 3 and 4 have additional parameter values nb and c, respectively, that have been tested on a range of values (see Section 3.3). In Table 2, we report the parameter values corresponding to the best-performing metric values of Fig. 6, i.e. again for the best-performing T_e field per model.

Table 2. Table containing the values of the best respective parameter value for Models 3 and 4 for the best-performing gas-saturation (S_g) value (see Section 4.4), i.e., number of blocks (nb) for Model 3 and c values for Model 4. The evaluation is based on Jaccard coefficient (J), Diffused Jaccard coefficient (low) (J_d^{low}), Diffused Jaccard coefficient (med) (J_d^{med}), and Diffused Jaccard coefficient (high) (J_d^{high}).

Injection rate	10ml/min		100ml/min		250ml/min		
Models	3	4	3	4	3	4	
Parameters	nb	c	nb	c	nb	c	
A	8	10	50	5	50	5	J
B	3	15	40	5	50	5	
C	5	5	30	5	50	5	
A	8	10	40	5	50	5	J_d^{low}
B	3	15	35	5	50	5	
C	5	5	30	5	50	5	
A	6	15	40	5	50	5	J_d^{med}
B	3	5	35	5	50	5	
C	3	200	30	5	40	5	
A	5	15	40	5	50	5	J_d^{high}
B	4	5	35	5	50	5	
C	3	10	30	5	40	5	

(Triplicate Experiments)

As anticipated in Section 3.3, at injection rates of 100 ml/min and 250 ml/min, Model 3 performs best with a higher number of blocks of invasion (see columns of 100 ml/min and 250 ml/min in Table 2). For Model 4, the best performing c values for injection rates of 100 ml/min and 250 ml/min are indeed the smallest on the list: $c = 5$ (see columns of 100 ml/min and 250 ml/min in Table 2), as already predicted in Section 3.3.

We observe that, for the injection rate of 10 ml/min, the best c values of Model 4 also correspond to the ones contributing to more inner randomness, i.e. the ones that assist in the radial spreading of the gas. This is unexpected at first sight: At an injection rate of 10ml/min, viscous effects exist but are not predominant, i.e. we observe less radial spreading in the experiments (top row of Fig. 2). We have observed similar be-

haviour in one of our earlier works (Banerjee, Walter, et al., 2023), where the experimental data belonged to the discontinuous gas flow regime.

Two opposing arguments are relevant to understand these surprisingly low c values at 10 ml/min. On the one hand, the higher c values (200 or 500) for a given invasion threshold are almost deterministic in their choice of the gas path. When these c values meet the entry threshold (T_e) field closest to the actual experiment conditions, the model can accurately produce the gas path with the highest similarity to the observed experimental gas finger. But for any threshold field with poor resemblance to the actual experimental conditions, models with these high c values produce poor-fitting gas fingers. On the other hand, models with lower c values are more flexible in their choice of a gas path for a given invasion threshold field (T_e). Combining the two arguments, these best-performing low c values indicate that, in the absence of a good fit of the structure of the T_e field to the experimental porous medium, the more flexible models fare well.

4.1.2 Relative Performance of the Models across 500 Runs.

Until now, we have discussed the model performance based on the overall maximum metric value out of the 500 runs. To analyse the relative performance of the model versions and sub-versions (with varying parameters, see Section 3.3) across 500 runs per metric value, we inspect the percentage of ranks obtained by each of them. We present a few plots to aid our discussion in Figs. 7 and 8. Please note that these rankings are relative among the models (and model sub-versions) per individual experiment, and it thus does not indicate whether any of these models best fit the experiments used in this study.

We observe from the rank-plots of experiments 10-A, 10-B, and 250-A using the Jaccard coefficient (Fig. 7, top row, and Fig. 8 top), that the Models 1 and 2 rank mediocre to poor amongst all the model (sub-) versions. Further, we notice that the best model according to the overall maximum metric value (Model 3, see table specified by Fig. 6) does not consistently rank well for all the 500 T_e fields (This becomes visible by the presence of red colour in the bars of Model 3 sub-versions in Fig. 7 and 8). This indicates that the T_e field is an essential input for these models, which will be further discussed in Section 4.3.
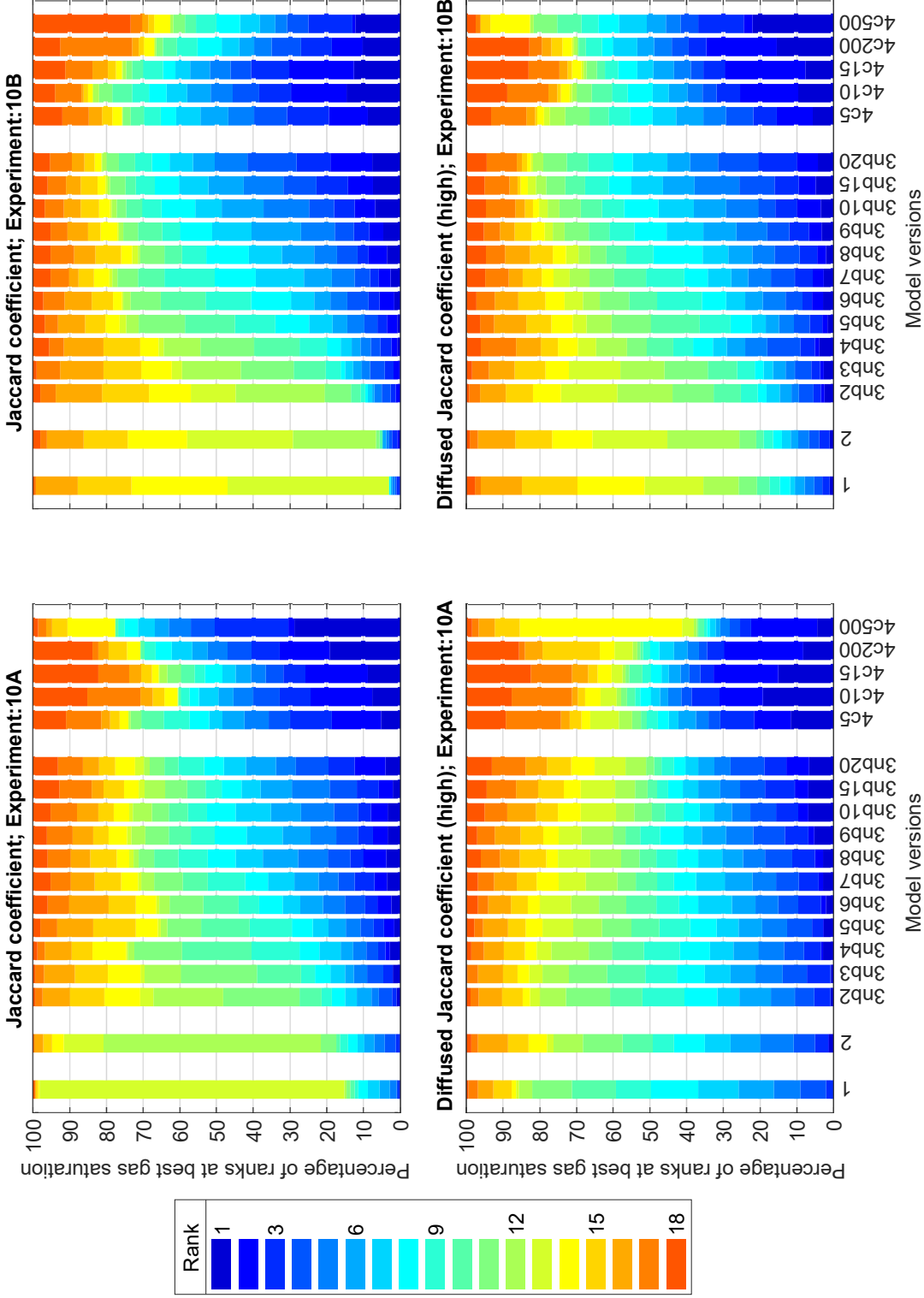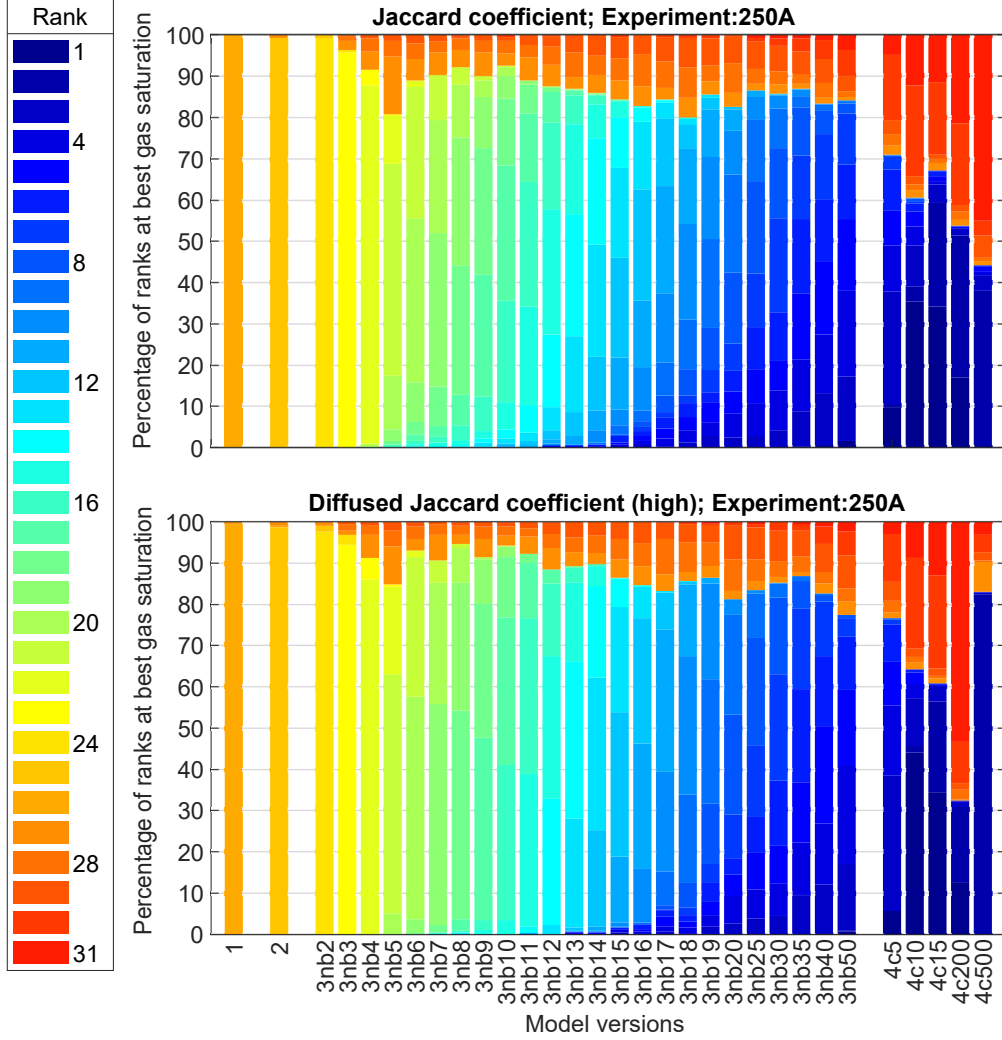
Figure 7. Bar plot of the percentage of relative ranks obtained by each model version out of the 500 runs for the best performing gas-saturation value for the corresponding run. The plots are for experiment numbers 10-A and 10-B, and the corresponding metrics used for ranking are mentioned in the title of the subplots. Labels 1 and 2 correspond to Models 1 and 2 of this study. The label 3nb2, 3nb3,... stands for Model 3 with $nb = 2, 3, ...$ invaded blocks and the label 4c5, 4c10,... stands for Model 4 with $c = 5, 10, ...$ respectively.

Figure 8. Bar plot of the percentage of relative ranks obtained by each model version out of the 500 runs for the best performing gas-saturation value for the corresponding run. The experiment number 250-A and the corresponding metric used for ranking are mentioned in the title of the subplots. Labels 1 and 2 correspond to Models 1 and 2 of this study. The label 3nb2, 3nb3.... stands for Model 3 with $nb = 2, 3, ...$ invaded blocks and the label 4c5, 4c10,... stands for Model 4 with $c = 5, 10, ...$ respectively.

Also, we notice that Model 4 with larger c values representing more systematic behaviour (relying primarily on the T_e field) ranks the best for 10-A (e.g., see bars 4c200 or 4c500 of the top row, left plot in Fig. 7), and those with c values representing somewhat directionless randomness to partially overrule the T_e field, rank better for 10-B (e.g., see bars 4c5 or 4c10 of the top row, right plot in Fig. 7). In the experimental results of 10-B, the gas finger moves towards the right boundary of the domain, indicating the significant influence of the T_e field in this experiment compared to 10-A where the gas moves through the centre of the domain (see Fig. 2). The probability of a random T_e field leading to a good match with that of experiment 10-B is extremely low. To overcome this large uncertainty in the T_e field in our models, the more flexible models (with more randomness at lower c values) perform better. In an overall conclusion, the T_e field matters for all models investigated here.

For higher injection rates, Model 4 with different c values ranks the best for some realizations and worst for others (e.g., the red-blue bars from the top plot in Fig. 8). This confirms our earlier impression that these models have gas finger patterns resembling the experimental images only when accompanied by "good" T_e fields. With T_e fields far away from that of the experiment, these models perform the worst. Hence, the "very good" Model 4 is highly sensitive to the T_e field input.

Blurring the images (i.e. comparisons at larger scales) makes the ranking less strict. Even weak models like 1 and 2 rank well for a higher percentage of times (see bottom row plots in Fig. 7) than they do for the non-blurred image comparison, i.e. using the plain Jaccard coefficient. However, for a high injection rate, blurring cannot help these models improve their ranking (bottom plot for Fig. 8) because the models are missing surrogate processes for viscosity, which is essential in this flow regime. The extensions proposed in Models 3 and 4 in this regard perform well.

4.2 Detailed Discussion of the Model Selection Results

We further support the rankings observed in Section 4.1 with more visual evidence and provide insights into the performance of the individual model (with its best T_e field).

Comparing the images (both blurred and non-blurred) of experiment 100-A and 250-A of Fig. 4 to outputs from Model 1 and Model 2 (Fig. 9), one can see that they are incapable of producing branched gas-finger patterns resembling those from exper-

iments at higher injection rates. Even with a high blurring radius, Model 1 and Model 2 produce patterns very different from the experiments at 100ml/min or 250ml/min, simply because they are incapable of having high volumes of gas in the domain. We would refer the reader to the supplementary information of this manuscript for more visual evidence.

Model 3, which emerges as the best model for almost all the metrics and experiments in Section 4.1, has more gas in the system (with many gas-occupied blocks in the domain) (Row 3 and columns 2 and 3 of Fig. 9). This is why it matches the higher injection rate experimental images better than Models 1 and 2.

The experimental images for triplicate at any particular injection rate differ in structure. Even with very high blurring, experimental images from 250-A (Fig. 4) and from 250-C (Fig. S2) have different patterns. This difference is not observed in the respective best-fitting outputs from Model 3 (see Fig. 10 and Fig. S13). The gas finger patterns produced by Model 3 are hardly distinct from one another (see Fig. 10).

Model 4, due to the inherent randomness in the invasion decision, can have many gas-occupied blocks within the domain (Row 4 and columns 2 and 3 of Fig. 9), facilitating a lateral spread of gas. However, unlike Model 3, it produces distinctive patterns. For example, in Fig. 10, the best-fitting Model 4 outputs to the various blurred versions of the experimental image of 250-A are not all alike. Note that although the patterns are distinct, they are not always completely similar to the experimental image.

Therefore, we again recommend that Model 1 and Model 2 should not be used for transitional or continuous gas flow regimes. Model 3 can be used for the transitional gas flow regime (with single, slightly thick fingers). At higher flow rates with many-branched fingers (continuous flow regime), Model 3 can be used at large scales (with blurring), but *with caution*: Model 3 is not capable of differentiating between different gas cluster shapes and structures. Thus, using Model 3 in the continuous regime will likely misrepresent gas volumes, pathways, and gas-water contact with associated effects on storage and mass transfer estimates. The close runner-up model (Model 4) is a suitable candidate for use in transitional and continuous flow regimes (identifying the different shapes of gas clusters), but the underlying rules need to be modified to closely match the gas flow processes involved at high injection rates, which is beyond the scope of the present work.
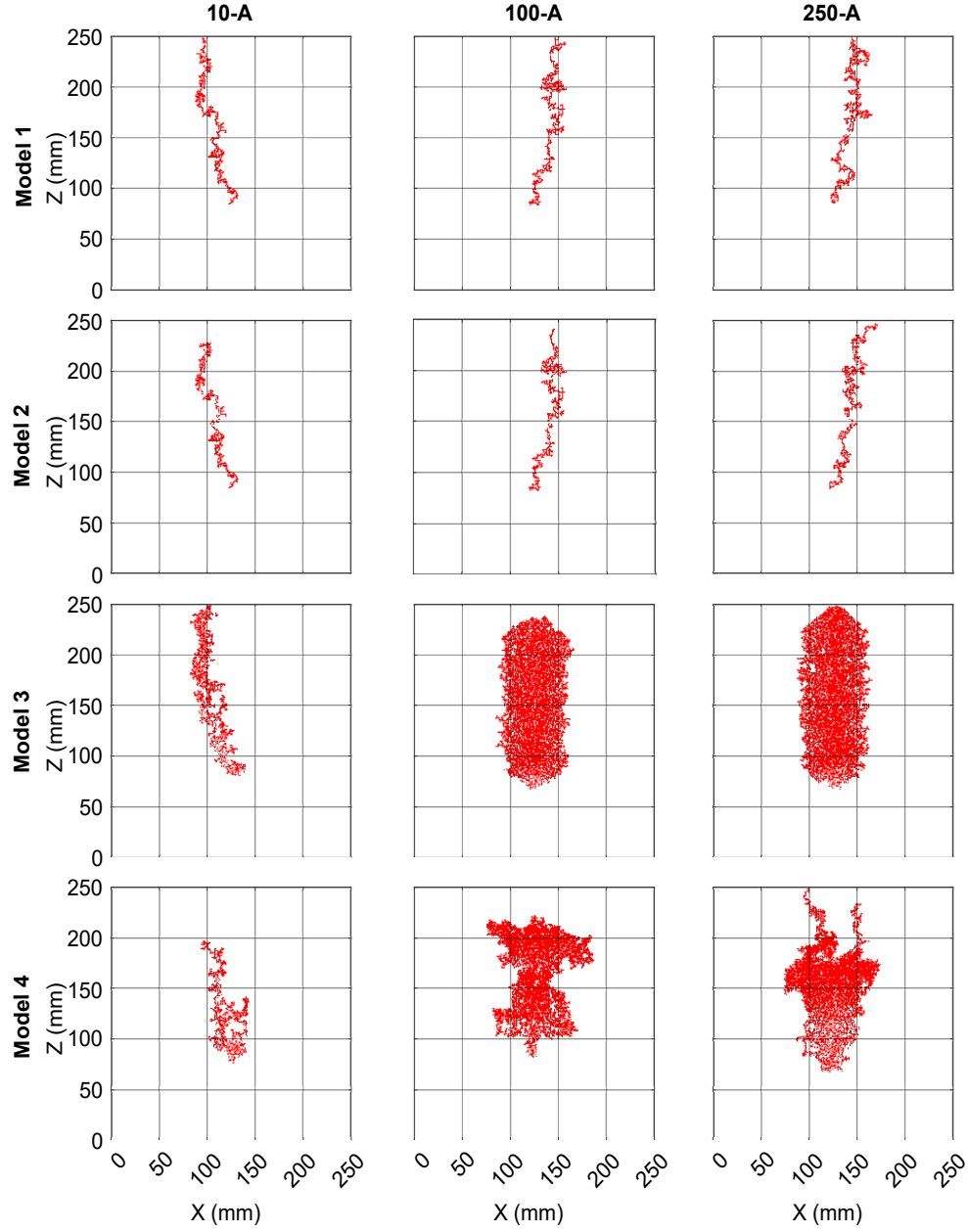
Figure 9. Model images for the different model versions with the best fit to non-blurred experimental images (with highest Jaccard value) from experiment no. 10-A, 100-A and 250-A. Row 1, Row 2, Row 3 and Row 4 correspond to Model 1, Model 2, Model 3 and Model 4, respectively.
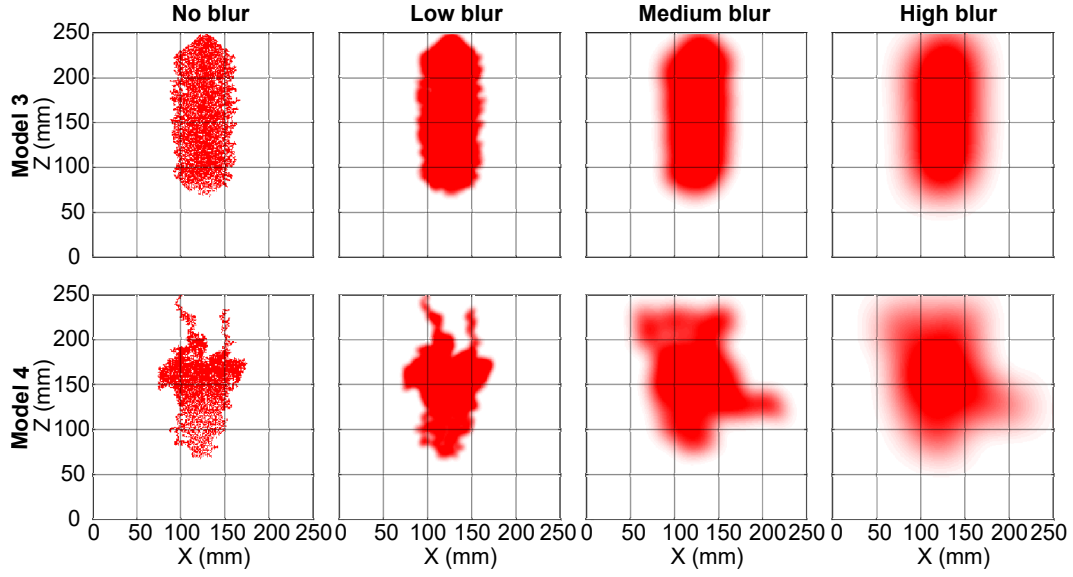
Figure 10. Best-fit model images for Models 3 and 4 relative to non-blurred and blurred versions of experimental image 250-A.

4.3 Importance of the Entry Threshold Fields

From the discussions in the sections above, it is clear that the underlying structure of the T_e field is an important input for these models. Recall that each of the best-performing metrics in Fig. 6 corresponds to a best-fitting T_e field. *Are there any similarities in the structures of these otherwise random best-fitting T_e fields for the different models?* We try to identify one path of least resistance through the T_e fields by running Model 1 on them. This means that Model 1 runs on the best T_e field for each model version evaluated using the maximum Jaccard coefficient. We choose Model 1 because, in it, all parameters except the T_e field are assumed fixed. The overlay of the so-obtained gas fingers on the experimental image shows that they partially cover the actual paths of the gas finger (Fig. 11). This answers the question pertaining to the similarities in the underlying structure of the best-fitting T_e fields.

Further, this observation (from Fig. 11) provides strategies to handle the importance of the T_e fields in spite of its uncertainty for these models. The strategy of Trevisan et al. (2017) was to run their IP model over multiple realisations of their T_e field to account for the uncertainty of the geological heterogeneity in their experimental setup. This seems a viable approach in this regard. Additionally, our comparison metric can be used to identify the "good performing" T_e fields for each model type. One could operate a (geo-
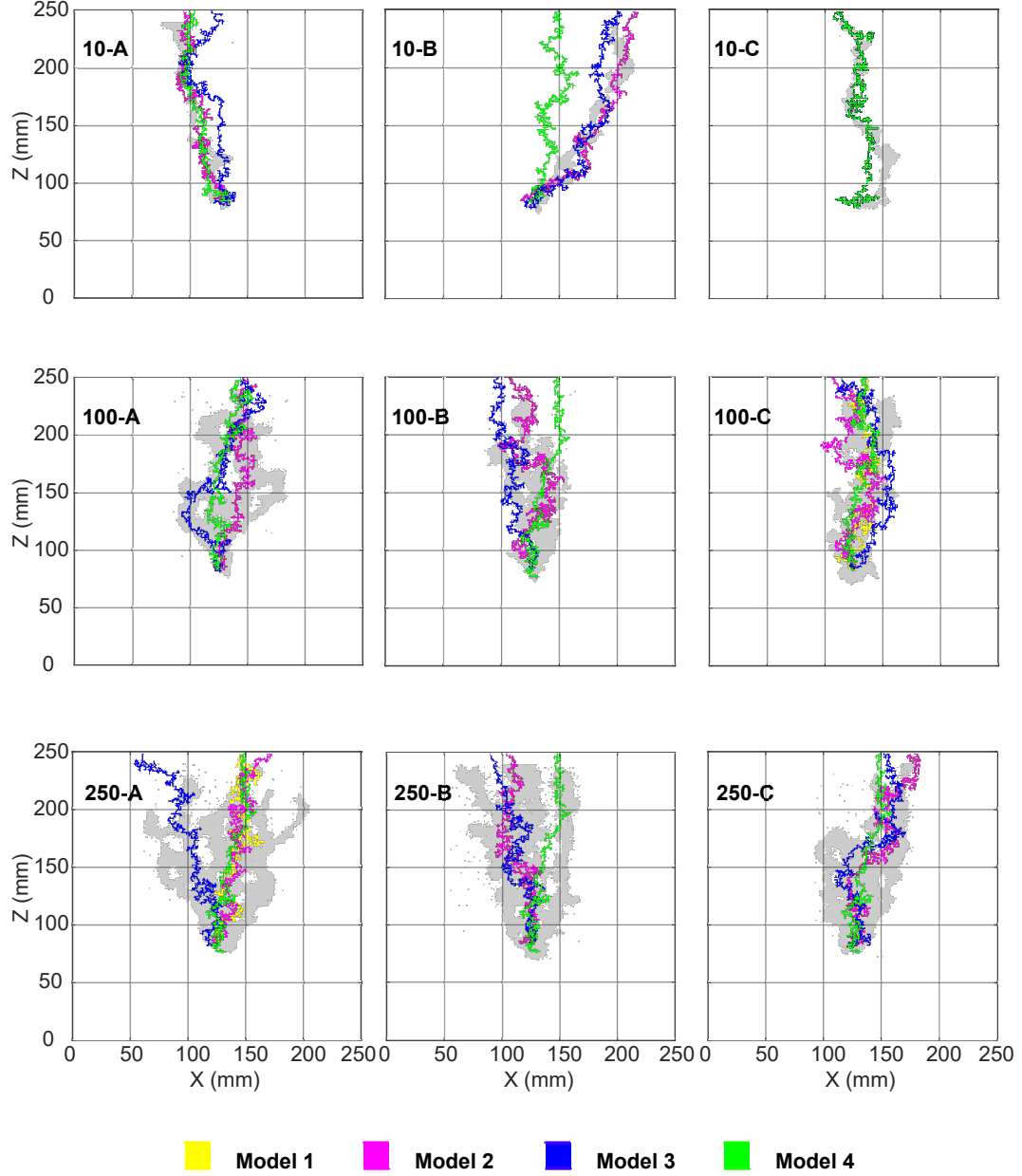
Figure 11. Figure shows the T_e field chosen for the maximum Jaccard coefficient per model version. It is produced using Model 1, in which only T_e fields vary; the other parameters are constant. Grey-coloured gas fingers represent the experimental image. Please note that each of the nine images has five different coloured fingers. The colours not visible in any of the sub-images are due to the overlap of pixels.

675 statistical) Bayesian inference to estimate (or conditionally simulate) the T_e fields, e.g.,

676 using Markov chain- Monte Carlo (MCMC) methods for random fields (Xu et al., 2020),

677 a parameter Ensemble Kalman filter (EnKf) (e.g., Kalman Ensemble generator by Nowak

678 (2009)) or transformed versions (Schöniger et al., 2012).

4.4 Best-fitting Gas Saturation Values

680 Recall that the results presented in the table specified by Fig. 6 used the best-fitting

681 gas saturation values (S_g) resulting from the time matching procedure per model and

682 realization (of T_e field). Now, we investigate these best-fitting S_g values out of our pro-

683 posed range for each model per metric (Section 3.3). Remember that our experimental

684 data and model outputs are binary (gas-presence/gas-absence) images. The gas satu-

685 ration values are an overall value provided to the entire gas cluster, i.e. all gas blocks

686 in the binary image are replaced by the same gas saturation value. Varying the gas-saturation

687 value varies the V_{mod} in Equation 11, thus altering the corresponding time-matched im-

688 age from the model outputs. Thus, the value of the metric changes when we change the

689 gas-saturation value. In Table A1 of Appendix A, we present the best-performing gas-

690 saturation values corresponding to the best metric values for the three experimental trip-

691 licate (table specified by Fig. 6). While some of the gas-saturation values reported in

692 Table A1 are comparable to those found in the experimental data, some are infeasible.

693 For example, a value of $S_g = 0.02$ (appears multiple times in Table A1) for the entire

694 gas cluster is clearly too low.

695 We further investigate the distribution of the gas saturation (S_g) values per model

696 (sub-) version for all 500 T_e field realizations. For that, we present a sample of nine scat-

697 ter plots for S_g (matched per T_e field realization), versus the metric (Jaccard coefficient

698 and Diffused Jaccard coefficient (high)) for selected models (Model 1, Model 3 and Model 4)

699 and experiments 10-A, 100-A, and 250-A in Fig. 12. We pick the sub-versions of Mod-

700 els 3 and 4 with the best-performing parameter values: nb and c, for the corresponding

701 cases (see Table 2).

702 There is no clear optimal value of S_g, i.e. the values do not show a cluster of points

703 at an exceptionally high metric value for any particular S_g value (see Figs. 12**a**, 12**b**, 12**c**,

704 12**f**, 12**g** and 12**h**). It instead seems to be an individual choice of these models per T_e

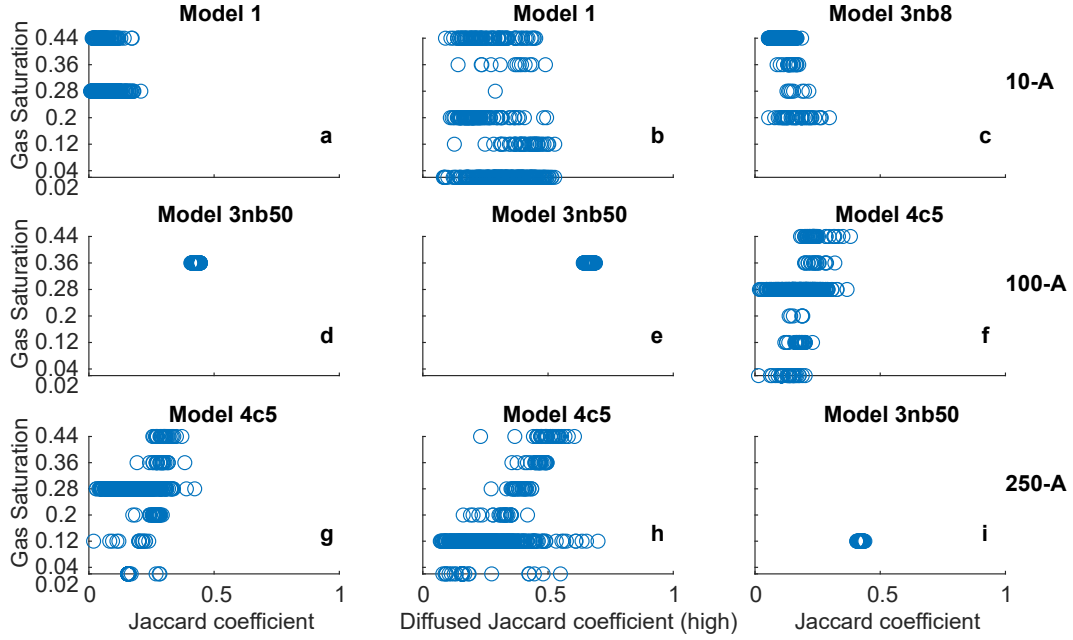705 field. For example, in the case of non-blurred images (evaluation using J), more strict

Figure 12. A sample of nine plots showing the gas saturation distribution per model (sub-) version for all 500 realizations over the respective metric values for experiments 10-A, 100-A and 250-A. The title of the subplots 3nb8 and 3nb50 stands for Model 3 with $nb = 8$ and $nb = 50$, respectively. The title of the subplots 4c5 stands for Model 4 with c value 5.

models (Models 1 and 2) stick to specific S_g values (see Fig. 12a). For blurred images of the same strict models, the spectrum of well-performing S_g values increases, but it still does not tend to one optimal value (see Fig. 12b). The blurring of the images spatially diffuses the pixels, and the actual structure of the gas finger becomes less relevant, which makes up for the conceptual weakness of Models 1 and 2, allowing them to cope with more varied S_g values. In other words, conceptually strong models are more flexible in their choice of S_g values. This is further supported by the observed spread of S_g values for Model 3 with $nb = 8$ (Fig. 12c), which produced a gas finger with a close resemblance to the original experimental image for 10-A (see Fig. 4 and 9).

In spite of the flexibility of choice of S_g values, conceptually strong models are expected to favour a particular S_g value. For Model 3, which ranks best in most scenarios of the table specified by Fig. 6, the sub-version with $nb = 50$ does favour a single S_g value (see Figs. 12d, 12e, and 12i). However, this optimal S_g value is not always realistic. For example, the converged S_g value for Model 3 with $nb = 50$ is 0.12 for experiment 250-A (see Fig. 12i). Van De Ven et al. (2020) reported typical S_g values be-

721 tween 0.20 to 0.4 for the inner core and 0.03 to 0.20 for the outer shell of each gas fin-

722 ger, from the high injection rate (100 ml/min, 250 ml/min and 498 ml/min) experimen-

723 tal triplicate of Van De Ven and Mumford (2019). Thus, the value of $S_g = 0.12$ for the

724 entire gas cluster is lower than that observed and reported in Van De Ven et al. (2020).

725 As earlier discussed in Section 4.2, Model 3 does not adequately predict the shape and

726 structure of the gas clusters consisting of multiple fingers. Thus, the favoured S_g value

727 is merely the model's best attempt to fit the corresponding data.

728 For the close runner-up Model 4 with $c = 5$, we do not observe any convergence

729 to an optimal S_g value (see Figs. 12**f**, 12**g**, and 12**h**). Recall that this model version's

730 performance is highly sensitive to the input of the entry threshold (T_e).

731 Therefore, the models apparently use the S_g values to compensate either for their

732 own conceptual weakness or for "poor" T_e field inputs. Thus, from Fig. 12, we can con-

733 clude that none of the models can predict the real physical S_g values and thus are not

734 recommended for S_g calibration. As a possible way out, one could develop data assim-

735 ilation or geostatistical inversion schemes for T_e fields as already mentioned in Section

736 4.3. Then, more plausible S_g values could be obtained as only the conceptual weakness

737 of models would remain as the major error source. Alternatively, model versions with

738 variable gas-saturated blocks (, e.g., Ioannidis et al., 1996; K. G. Mumford et al., 2010;

739 Koch & Nowak, 2015; Molnar et al., 2019) are an optional extension of macroscopic IP

740 models, which may be investigated for better calibration of S_g values.

4.5 Summary of Findings

741

742 We summarise that Models 1 and 2 are unsuitable for use in transitional and con-

743 tinuous gas flow regimes, even with high levels of blurring in images (Section 4.1). Mod-

744 els 3 and 4 perform better than Models 1 and 2 but do not accurately represent the gas

745 finger patterns observed in the experiments (Section 4.1 and 4.2). Model 3 is a good fit

746 for experiments in the transitional gas flow regime (single slightly thick gas finger) but

747 cannot appropriately predict the gas-finger patterns seen in the experiments of the con-

748 tinuous gas flow regime (multiple fingers) (Section 4.2). Model 4 is a potential candidate

749 for use in the transitional and continuous gas flow regimes, provided its rules are mod-

750 ified to reproduce the gas-flow behaviour at high injection rates (Section 4.2). The mod-

751 ification of Model 4's underlying rules is beyond the scope of the present study. With

blurring, i.e. at large scales where individual structures of the gas fingers are irrelevant, Models 3 and 4 may be used for continuous gas flow regimes (Section 4.1 and 4.2). Their use would thus depend on the application. We also identify that the structure of the T_e field is a critical input for a good performance of these models (Section 4.3). The internal randomness of the invasion decision can partially compensate for the high uncertainty in the structure of the T_e fields (Section 4.1 and 4.2). Also, strategies like running multiple realizations of the T_e field can help tackle this uncertainty of the T_e fields. Further, we do not recommend these models for calibrating parameters like gas saturation (Section 4.4), at least as long as there is a dominant uncertainty in T_e fields.

5 Conclusions and Outlook

We compared the performance of four macroscopic IP models against the data from nine experiments. The experiments featured gas injections in homogeneous water-saturated sand. For comparison, we used time-matching and (Diffused) Jaccard coefficient(s). For the first time, these models are tested for transitional and continuous gas-flow regimes. We identified the strengths and weaknesses of these modelling strategies for simulating gas flow in water-saturated sand. Also, we calibrated a few parameters of these models.

We conclude that Models 1 and 2 should not be used for the transitional and continuous regimes of gas flow discussed in this study. In particular, for experiments at higher injection rates, these models are completely weak. In previous studies, IP models have been used extensively only in the capillary flow domain. Our results show that IP models at a macroscopic scale with variation as Model 3 can be used in the transitional gas flow regime but is unfit for use in the continuous gas flow regime. In their present state, Models 3 and 4 can be used with blurring for large-scale applications in the continuous gas flow regime, where the details of the gas-cluster structure are insignificant. Thus, the exact use would depend on the specific application. Models 3 and 4 are better because they can partially consider the viscous effects found at high gas injection rates.

The blurring of images can be used as an efficient tool for reducing the detailed level of information in the images, depending on the application and the scale of interest. It is pointless to ask for a pixel-to-pixel match at and above the scale of the experiments used in this study, given the strong dependence of gas flow on pore-scale aspects of the

porous medium (here: sand pack). This exercise can thus help use models like 3 or 4 for such applications.

The underlying structure of the T_e fields is a critical input for these models. Moreover, the best models (3 or 4) are also the most sensitive to this input. Further research could be conducted to identify the underlying structure of the T_e fields, e.g., using geostatistical inversion methods.

Currently, Model 3 and Model 4 show some promise in performance, but further research towards refining their rules for gas-invasion, water-re-invasion, finger branching, and so on, needs to be done. A possible extension could be a mix of Model 3's rule of invading more blocks per step combined with a stochastic invasion rule similar to that of Model 4. The rule for this extension would also need to be adapted to closely mimic the gas flow behaviour in the continuous flow regime, e.g., with finger invasion rules enabling the growth of multiple parallel thick fingers.

Appendix A Gas Saturation Values

The table containing the best-performing gas-saturation values per model version per experiment and for each metric used in this study:

Table A1. Table containing gas saturation values corresponding to the maximum metric value, Jaccard coefficient (J), Diffused Jaccard coefficient (low) (J_d^{low}), Diffused Jaccard coefficient (med) (J_d^{med}), and Diffused Jaccard coefficient (high) (J_d^{high}).

Injection rate		10 ml/min				100ml/min				250ml/min			
	Models	1	2	3	4	1	2	3	4	1	2	3	4
J	A	0.28	0.28	0.20	0.36	0.28	0.36	0.36	0.44	0.12	0.12	0.12	0.28
	B	0.28	0.28	0.36	0.44	0.36	0.36	0.44	0.28	0.12	0.12	0.12	0.28
	C	0.28	0.28	0.36	0.44	0.36	0.36	0.44	0.28	0.28	0.28	0.12	0.28
J_d^{low}	A	0.44	0.02^a	0.20	0.28	0.28	0.28	0.44	0.44	0.02^a	0.02^a	0.44	0.28
	B	0.02^a	0.02^a	0.36	0.44	0.36	0.36	0.44	0.44	0.28	0.28	0.28	0.20
	C	0.20	0.20	0.36	0.20	0.28	0.28	0.44	0.02^a	0.28	0.28	0.28^b	0.28
J_d^{med}	A	0.44	0.20	0.20	0.20	0.28	0.28	0.44	0.02^a	0.02^a	0.02^a	0.20	0.02^a
	B	0.20	0.20	0.36	0.12	0.28	0.28	0.44	0.44	0.02^a	0.02^a	0.12	0.12
	C	0.20	0.20	0.20	0.44	0.20	0.20	0.44	0.36	0.02^a	0.02^a	0.02^a	0.02^a
J_d^{high}	A	0.12	0.36	0.20	0.20	0.44	0.02^a	0.44	0.44	0.12	0.12	0.36	0.12
	B	0.44	0.36	0.12	0.20	0.12	0.12	0.44	0.44	0.20	0.02^a	0.12^c	0.12
	C	0.36	0.20	0.28	0.02^a	0.36	0.02^a	0.44	0.02^a	0.36	0.12	0.02^a	0.12

(Row group: Triplicate Experiments)

[a] Same metric values also obtained for a gas saturation value of 0.04

[b] Same metric values also obtained for a gas saturation value of 0.36

[c] Same metric values also obtained for a gas saturation value of 0.20

Data availability:

The experimental data used in this study is available at: `https://doi.org/10.5683/SP3/A7ITKL` (K. Mumford, 2023).

The modelling data and codes used for this study are available in the DaRUS dataverse for Stochastic Simulation and Safety Research for Hydrosystems (LS3): `https://darus.uni-stuttgart.de/privateurl.xhtml?token=22c4714c-0dd2-4d57-9a95-d3b16c544b40` (Banerjee, Guthke, & Nowak, 2023). It will be made public upon acceptance.

References

Banerjee, I., Guthke, A., & Nowak, W. (2023). *Replication Data for: Comparison of Four Competing Invasion Percolation Models for Gas flow in Porous Media.* DaRUS (Draft Version). doi: 10.18419/darus-3592

Banerjee, I., Guthke, A., Van De Ven, C. J. C., Mumford, K. G., & Nowak, W. (2021). Overcoming the model-data-fit problem in porous media: A quantitative method to compare invasion-percolation models to high-resolution data. *Water Resources Research*, *57*. doi: 10.1029/2021WR029986

Banerjee, I., Walter, P., Guthke, A., Mumford, K. G., & Nowak, W. (2023). The method of forced probabilities: a computation trick for bayesian model evidence. *Computational Geosciences*, *27*, 45-62. doi: 10.1007/s10596-022-10179-x

Ben-Noah, I., Friedman, S. P., & Berkowitz, B. (2022). Air injection into water-saturated granular media—a dimensional meta-analysis. *Water Resources Research*, *58*(6), e2022WR032125. Retrieved from `https://agupubs.onlinelibrary.wiley.com/doi/abs/10.1029/2022WR032125`

830   (e2022WR032125 2022WR032125) doi: 10.1029/2022WR032125

831   Birovljev, A., Furuberg, L., Feder, J., Jssang, T., Mly, K. J., & Aharony, A.   (1991).

832   Gravity invasion percolation in two dimensions: Experiment and simulation.

833   *Physical Review Letters*, *67*, 584-587. doi: 10.1103/PhysRevLett.67.584

834   Broadbent, S. R., & Hammersley, J. M.   (1957).   Percolation processes: I. crystals

835   and mazes.   *Mathematical Proceedings of the Cambridge Philosophical Society*,

836   *53*(3), 629–641. doi: 10.1017/S0305004100032680

837   Brooks, M. C., Wise, W. R., & Annable, M. D.   (1999).   Fundamental changes in

838   in situ air sparging flow patterns.   *Groundwater Monitoring & Remediation*,

839   *19*(2), 105-113. doi: 10.1111/j.1745-6592.1999.tb00211.x

840   Brooks, R., & Corey, A.   (1964).   Hydraulic properties of porous media.   *Hydrology*

841   *Papers, Colorado State University*, 4.

842   Cavanagh, A. J., & Haszeldine, R. S.   (2014).   The sleipner storage site: Capil-

843   lary flow modeling of a layered co2 plume requires fractured shale barriers

844   within the utsira formation. *International Journal of Greenhouse Gas Control*,

845   *21*, 101-112.   Retrieved from `https://www.sciencedirect.com/science/`

846   `article/pii/S1750583613004192`   doi: 10.1016/j.ijggc.2013.11.017

847   Deza, M. M., & Deza, E. (2016). *Encyclopedia of Distances*. Springer-Verlag, Berlin,

848   Heidelberg. doi: 10.1007/978-3-662-52844-0

849   Ewing, R. P., & Berkowitz, B.   (1998).   A generalized growth model for simulat-

850   ing initial migration of dense non-aqueous phase liquids.   *Water Resources Re-*

851   *search*, *34*, 611–622. doi: 10.1029/97WR03754

852   Ewing, R. P., & Berkowitz, B.   (2001).   Stochastic pore-scale growth models of

853   DNAPL migration in porous media.   *Advances in Water Resources*.   doi:

854   10.1016/S0309-1708(00)00059-2

855   Ewing, R. P., & Gupta, S. C.   (1993).   Modeling percolation properties of random

856   media using a domain network.   *Water Resources Research*, *29*(9), 3169-3178.

857   Retrieved from `https://agupubs.onlinelibrary.wiley.com/doi/abs/`

858   `10.1029/93WR01496`   doi: 10.1029/93WR01496

859   Frette, V., Feder, J., Jøssang, T., & Meakin, P. (1992). Buoyancy-driven fluid migra-

860   tion in porous media.   *Physical Review Letters*.   doi: 10.1103/PhysRevLett.68

861   .3164

862   Geistlinger, H., Krauss, G., Lazik, D., & Luckner, L.   (2006).   Direct gas in-

jection into saturated glass beads: Transition from incoherent to coherent gas flow pattern. *Water Resources Research*, *42*(7), 1–12. doi: 10.1029/2005WR004451

Gerhard, J. I., & Kueper, B. H. (2003). Capillary pressure characteristics necessary for simulating DNAPL infiltration, redistribution, and immobilization in saturated porous media. *Water Resources Research*. doi: 10.1029/2002WR001270

Glass, R. J., Conrad, S. H., & Peplinski, W. (2000). Gravity-destabilized nonwetting phase invasion in macroheterogeneous porous media: Experimental observations of invasion dynamics and scale analysis. *Water Resources Research*, *36*(11), 3121-3137. Retrieved from `https://agupubs.onlinelibrary.wiley.com/doi/abs/10.1029/2000WR900152` doi: 10.1029/2000WR900152

Glass, R. J., Conrad, S. H., & Yarrington, L. (2001). Gravity-destabilized nonwetting phase invasion in macroheterogeneous porous media: Near-pore-scale macro modified invasion percolation simulation of experiments. *Water Resources Research*, *37*(5), 1197–1207. doi: 10.1029/2000WR900294

Glass, R. J., & Nicholl, M. (1996). Physics of gravity fingering of immiscible fluids within porous media: An overview of current understanding and selected complicating factors. *Geoderma*, *70*(2), 133-163. doi: 10.1016/0016-7061(95)00078-X

Glass, R. J., & Yarrington, L. (1996). Simulation of gravity fingering in porous media using a modified invasion percolation model. *Geoderma*, *70*(2), 231-252. Retrieved from `https://www.sciencedirect.com/science/article/pii/0016706195000879` doi: 10.1016/0016-7061(95)00087-9

Glass, R. J., & Yarrington, L. (2003). Mechanistic modeling of fingering, non-monotonicity, fragmentation, and pulsation within gravity/buoyant destabilized two-phase/unsaturated flow. *Water Resources Research*, *39*(3). doi: 10.1029/2002WR001542

Held, R. J., & Illangasekare, T. H. (1995). Fingering of dense nonaqueous phase liquids in porous media: 2. analysis and classification. *Water Resources Research*, *31*(5), 1223-1231. Retrieved from `https://agupubs.onlinelibrary.wiley.com/doi/abs/10.1029/95WR00429` doi: 10.1029/95WR00429

Ioannidis, M. A., Chatzis, I., & Dullien, F. A. L. (1996). Macroscopic percolation model of immiscible displacement: Effects of buoyancy and spatial structure.

Water Resources Research, *32*(11), 3297-3310. doi: 10.1029/95WR02216

Ji, W., Dahmani, A., Ahlfeld, D. P., Lin, J. D., & Hill III, E. (1993). Laboratory study of air sparging: Air flow visualization. *Groundwater Monitoring & Remediation*, *13*(4), 115-126. doi: 10.1111/j.1745-6592.1993.tb00455.x

Kechavarzi, C., Soga, K., & Wiart, P. (2000). Multispectral image analysis method to determine dynamic fluid saturation distribution in two-dimensional three-fluid phase flow laboratory experiments. *Journal of Contaminant Hydrology*. doi: 10.1016/S0169-7722(00)00133-9

Koch, J., & Nowak, W. (2015). Predicting dnapl mass discharge and contaminated site longevity probabilities: Conceptual model and high-resolution stochastic simulation. *Water Resources Research*, *51*(2), 806-831. Retrieved from https://agupubs.onlinelibrary.wiley.com/doi/abs/10.1002/2014WR015478 doi: 10.1002/2014WR015478

Kueper, B. H., & McWhorter, D. B. (1992). The use of macroscopic percolation theory to construct large-scale capillary pressure curves. *Water Resources Research*. doi: 10.1029/92WR01176

Lenormand, R., Touboul, E., & Zarcone, C. (1988). Numerical models and experiments on immiscible displacements in porous media. *Journal of Fluid Mechanics*, *189*(November), 165–187. doi: 10.1017/S0022112088000953

Løvoll, G., Méheust, Y., Måløy, K. J., Aker, E., & Schmittbuhl, J. (2005). Competition of gravity, capillary and viscous forces during drainage in a two-dimensional porous medium, a pore scale study. *Energy*, *30*(6), 861-872. (Second International Onsager Conference) doi: 10.1016/j.energy.2004.03.100

Meakin, P., & Deutch, J. M. (1986). The formation of surfaces by diffusion limited annihilation. *The Journal of Chemical Physics*, *85*(4), 2320-2325. Retrieved from https://doi.org/10.1063/1.451129 doi: 10.1063/1.451129

Meakin, P., Feder, J., Frette, V., & Jo/ssang, T. (1992, Sep). Invasion percolation in a destabilizing gradient. *Phys. Rev. A*, *46*, 3357–3368. Retrieved from https://link.aps.org/doi/10.1103/PhysRevA.46.3357 doi: 10.1103/PhysRevA.46.3357

Molnar, I. L., Mumford, K. G., & Krol, M. M. (2019). Electro-thermal subsurface gas generation and transport: Model validation and implications. *Water Resources Research*, *55*, 4630-4647. doi: 10.1029/2018WR024095

Morrow, N. R. (1979, 07). Interplay of Capillary, Viscous And Buoyancy Forces In the Mobilization of Residual Oil. *Journal of Canadian Petroleum Technology*, *18*(03). Retrieved from https://doi.org/10.2118/79-03-03 doi: 10.2118/79-03-03

Mumford, K. (2023). *Replication Data for: Comparison of four competing invasion percolation models for gas flow in porous media.* Borealis. doi: 10.5683/SP3/A7ITKL

Mumford, K. G., Dickson, S. E., & Smith, J. E. (2009). Slow gas expansion in saturated natural porous media by gas injection and partitioning with non-aqueous phase liquids. *Advances in Water Resources*, *32*(1), 29–40. doi: 10.1016/j.advwatres.2008.09.006

Mumford, K. G., Hegele, P. R., & Vandenberg, G. P. (2015). Comparison of Two-Dimensional and Three-Dimensional Macroscopic Invasion Percolation Simulations with Laboratory Experiments of Gas Bubble Flow in Homogeneous Sands. *Vadose Zone Journal*, *14*(11), 0. doi: 10.2136/vzj2015.02.0028

Mumford, K. G., Smith, J. E., & Dickson, S. E. (2010). The effect of spontaneous gas expansion and mobilization on the aqueous-phase concentrations above a dense non-aqueous phase liquid pool. *Advances in Water Resources*, *33*(4), 504–513. Retrieved from http://dx.doi.org/10.1016/j.advwatres.2010.02.002 doi: 10.1016/j.advwatres.2010.02.002

Niemet, M. R., & Selker, J. S. (2001). A new method for quantification of liquid saturation in 2D translucent porous media systems using light transmission. *Advances in Water Resources*, *24*(6), 651–666. doi: 10.1016/S0309-1708(00)00045-2

Nowak, W. (2009). Best unbiased ensemble linearization and the quasi-linear kalman ensemble generator. *Water Resources Research*, *45*(4). doi: 10.1029/2008WR007328

Oldenburg, C. M., Mukhopadhyay, S., & Cihan, A. (2016). On the use of darcy's law and invasion-percolation approaches for modeling large-scale geologic carbon sequestration. *Greenhouse Gases: Science and Technology*, *6*(1), 19-33. doi: 10.1002/ghg.1564

Paterson, L. (1984, Apr). Diffusion-limited aggregation and two-fluid displacements in porous media. *Phys. Rev. Lett.*, *52*, 1621–1624. Retrieved

from `https://link.aps.org/doi/10.1103/PhysRevLett.52.1621`   doi: 10.1103/PhysRevLett.52.1621

Samani, S., & Geistlinger, H.   (2019).   Simulation of channelized gas flow pattern in heterogeneous porous media: A feasibility study of continuum simulation at bench scale.   *Vadose Zone Journal*, *18*(1), 180144.   Retrieved from `https://acsess.onlinelibrary.wiley.com/doi/abs/10.2136/vzj2018.07.0144`   doi: 10.2136/vzj2018.07.0144

Schöniger, A., Nowak, W., & Hendricks Franssen, H.-J.   (2012).   Parameter estimation by ensemble kalman filters with transformed data: Approach and application to hydraulic tomography.   *Water Resources Research*, *48*(4).   doi: 10.1029/2011WR010462

Schroth, M. H., Istok, J. D., Ahearn, S. J., & Selker, J. S.   (1996).   Characterization of miller-similar silica sands for laboratory hydrologic studies.   *Soil Science Society of America Journal*, *60*, 1331-1339.   doi: 10.2136/sssaj1996.03615995006000050007x

Selker, J. S., Niemet, M., Mcduffie, S. M., Norton G.and Gorelick, & Parlange, J.-Y.   (2006).   The local geometry of gas injection into saturated homogeneous porous media.   *Transp Porous Med*, *68*, 107-127.   doi: 10.1007/s11242-006-0005-0

Stöhr, M., & Khalili, A.   (2006, Mar).   Dynamic regimes of buoyancy-affected two-phase flow in unconsolidated porous media.   *Phys. Rev. E*, *73*, 036301.   doi: https://10.1103/PhysRevE.73.036301

Tidwell, V. C., & Glass, R. J.   (1994).   X ray and visible light transmission for laboratory measurement of two-dimensional saturation fields in thin-slab systems.   *Water Resources Research*, *30*(11), 2873–2882.   doi: 10.1029/94WR00953

Trevisan, L., Illangasekare, T. H., & Meckel, T. A.   (2017).   Modelling plume behavior through a heterogeneous sand pack using a commercial invasion percolation model.   *Geomechanics and Geophysics for Geo-Energy and Geo-Resources*, *3*, 327-337.   doi: 10.1007/s40948-017-0055-5

Tsimpanogiannis, I. N., & Yortsos, Y. C.   (2004).   The critical gas saturation in a porous medium in the presence of gravity.   *Journal of Colloid and Interface Science*.   doi: 10.1016/j.jcis.2003.09.036

Van De Ven, C. J., Abraham, J. E., & Mumford, K. G.   (2020).   Laboratory investigation of free-phase stray gas migration in shallow aquifers

using modified light transmission. *Advances in Water Resources*. doi: 10.1016/j.advwatres.2020.103543

Van De Ven, C. J., & Mumford, K. G. (2019). Characterization of gas injection flow patterns subject to gravity and viscous forces. *Vadose Zone Journal*, *18*(1), 1–11. doi: 10.2136/vzj2019.02.0014

Wagner, G., Meakin, P., Feder, J., & Jøssang, T. (1997). Buoyancy-driven invasion percolation with migration and fragmentation. *Physica A: Statistical Mechanics and its Applications*, *245*(3-4), 217–230. doi: 10.1016/S0378-4371(97)00324 -5

Wilkinson, D. (1984). Percolation model of immiscible displacement in the presence of buoyancy forces. *Physical Review A*. doi: 10.1103/PhysRevA.30.520

Wilkinson, D., & Willemsen, J. F. (1983). Invasion percolation: A new form of percolation theory. *Journal of Physics A: Mathematical and General*. doi: 10 .1088/0305-4470/16/14/028

Witten, T. A., & Sander, L. M. (1983, May). Diffusion-limited aggregation. *Phys. Rev. B*, *27*, 5686–5697. Retrieved from `https://link.aps.org/doi/10.1103/ PhysRevB.27.5686` doi: 10.1103/PhysRevB.27.5686

Xu, T., Reuschen, S., Nowak, W., & Hendricks Franssen, H.-J. (2020). Preconditioned crank-nicolson markov chain monte carlo coupled with parallel tempering: An efficient method for bayesian inversion of multi-gaussian log-hydraulic conductivity fields. *Water Resources Research*, *56*(8), e2020WR027110. Retrieved from `https://agupubs.onlinelibrary.wiley.com/doi/abs/ 10.1029/2020WR027110` (e2020WR027110 10.1029/2020WR027110) doi: 10.1029/2020WR027110